Topology optimization of heat sinks for instantaneous chip cooling using a transient pseudo-3D thermofluid model

Zeng, Tao; Wang, Hu; Yang, Mengzhu; Alexandersen, Joe

Published in:
International Journal of Heat and Mass Transfer

DOI:
10.1016/j.ijheatmasstransfer.2020.119681

Publication date:
2020

Document version:
Accepted manuscript

Topology optimization of heat sinks for instantaneous chip cooling using a transient pseudo-3D thermofluid model

Tao Zeng[a *], Hu Wang[a Ψ], Mengzhu Yang[a], Joe Alexandersen[b]

[a] *State Key Laboratory of Advanced Design and Manufacturing for Vehicle Body, Hunan University, Changsha, 410082, PR China*

[b] *Department of Technology and Innovation, University of Southern Denmark, Odense, Denmark*

Abstract: With the increasing power density of electronics components, the heat dissipation capacity of heat sinks gradually becomes a bottleneck. Many structural optimization methods, including topology optimization, have been widely used for heat sinks. Due to its high design freedom, topology optimization is suggested for the design of heat sinks using a transient pseudo-3D thermofluid model to acquire better instantaneous thermal performance. The pseudo-3D model is designed to reduce the computational cost and maintain an acceptable accuracy. The model relies on an artificial heat convection coefficient to couple two layers and establish the approximate relationship with the corresponding 3D model. In the model, a constant pressure drop and heat generation rate are treated. The material distribution is optimized to reduce the average temperature of the base plate at the prescribed terminal time. Furthermore, to reduce the intermediate density regions during the density-based topology optimization procedure, a detailed analysis of interpolation functions is made and the penalty factors are chosen on this basis. Finally, considering the engineering application of the model, a practical model with more powerful cooling medium and higher inlet pressure is built. The optimized design shows a better instantaneous thermal performance and provides 66.7% of the pumping power reduction compared with reference design.

Keywords: Transient pseudo-3D; Thermofluid; Instantaneous thermal performance; Topology optimization

Nomenclature

[*] First author: T. Zeng. E-mail: zengtao123@hnu.edu.cn

[Ψ] Corresponding author: H. Wang, E-mail: wanghu@hnu.edu.cn

A	area
c	specific heat
C	ratio of properties of fluid phase and solid phase
C_h	heat capacity
Da	Darcy number
$d_{\min}$	minimum mesh size
E	pumping energy consumption
ES	pumping energy consumption rate
f	objective function
$\mathbf{f}$	source vector term in Navier-Stokes equations (2)
f_b	heat source of base plate
f_c	source term of energy conservation equation (4)
f_v	volume friction
h	heat exchange coefficient
I	interpolation function
I_s	interpolation function of product of density and specific heat interpolation functions
k	thermal conductivity
L_c	characteristic length
$\mathbf{n}$	unit normal vector
n_{ev}	maximum evaluation number
p	pressure
p_{drop}	pressure drop
P_{pump}	pumping power
q	penalty factors
$q_{bp,d}$	heat dissipating power directly from base plate to air
q_{fin}	heat dissipating power from heat sink fins to air
q_{in}	inner heat transferred between the channel layer and base plate layer
q_{out}	heat flux through the outlet
q_s	penalty factors of product of density and specific heat interpolation functions
Q	rate of heat production
r_{fil}	filter radius
$r_{\min}$	minimum radius
r_f	volumetric flow rate through inlet
s	product of density and specific heat
t	time
t_{bp}	thickness of heat sink base plate
t_{ch}	thickness of heat sink channel
T	temperature vector
T_b	temperature of base plate
$\mathbf{u}$	velocity vector
v	velocity magnitude

V	volume
$\mathbf{x}$	system coordinate vector

Greek symbols

α	inverse permeability
β	projection steepness parameter
$\overline{\alpha}$	maximum inverse permeability
γ	residual of the finite element formulation
ε	tolerance of optimization process
ρ	material density
θ	design variable
θ_0	initial value of design variable
μ	dynamic fluid viscosity
ψ	field variables vector
Ω	domain
Γ	domain boundary
η	projection threshold parameter
$\overline{\tilde{\theta}}$	projected design field

Subscripts

f	fluid phase
c	cooling procedure
ht	heating procedure
s	solid phase
in	inlet
out	outlet
bp	base plate
wet	regions where solid material is in contact with fluid
air	air
fin	heat sink fins
T	terminal point
α	inverse permeability
k	thermal conductivity
h	heat exchange coefficient
d	design (domain)
avg	average value of base plate (or chip)
hs	heat sink
opt	optimized model
reg	reference model

1. Introduction

Thermal management of electronics is becoming more and more challenging with the advancement of chips in miniaturization and performance. While two-phase cooling can reach extreme heat fluxes, its application is limited by the complexity of fabrication,

assembly and operation [1]. For instance, recent gaming central-processing-units (CPUs) such as Intel® Core™ i9-9900K are very popular among consumer chips. It has 8 cores (16 threads) and a 3.6GHz base frequency, but more importantly, it can overclock to over 5GHz. Although the gaming performance improves a lot, its Thermal Design Power (TDP) has reached 95W in a 37.5*mm*×37.5*mm*×1.15*mm* chip size, which brings challenges to heat dissipation. According to recent surveys in Intel® official website [2]，the chip turbo frequency condition has a limit temperature (junction temperature). When the temperature exceeds this temperature limit, the chip frequency will be actively reduced along with the chip's performance. To minimize the time of chip frequency reduction, an active cooling device is proposed to achieve the minimum temperature of the chip below the turbo temperature limit as fast as possible. The turbo temperature limit refers to the temperature limit, under which a given CPU works in overclocked conditions. This means that when the chip average temperature surpasses this limit, the CPU would actively decrease the working frequency (calculation ability). There exist two common types of active coolers: air-cooled heat sink and liquid-cooled heat sink. Liquid heat sinks are prohibitive for many consumers due to their high price and short service life. However, when using air-cooled heat sinks, it is hard to satisfy the heat dissipation requirement of high-performance chips like the Intel® Core™ i9-9900K. One of the efficient methods to improve the thermal performance of heat sink is structural optimization.

For the structural optimization of the chip heat sink, previous researchers proposed an oblique fin design [3] and wavy channel designs [4,5] for heat sinks. Bejan and Errera et al. [6] proposed convective trees of fluid channels. Another design approach inspired by natural structures is fractal-like flow networks: Taylor et al. [7] utilized the fractal-like branching in microchannel heat sink to reduce the pumping power and wall temperature in the system; Chen et al. [8] were inspired by the fractal pattern of mammalian circulatory and respiratory systems, and they also made a comparison of the new design with the traditional parallel net. Recently a novel concept for energy efficiency hotspot targeted liquid cooling of microprocessors was proposed by Sharma et al. [9] and they greatly reduced chip temperature non-uniformities. In addition to the new design of fins and channels and intuitive structures inspired by natural structures, shape optimization was implemented to multi-objective optimization of a heat exchanger with parallel genetic algorithms by Hilbert et al. [10].

Topology optimization is a higher-level structural optimization method originally introduced to design optimal topologies with a homogenization method by Bendsøe et al. [11]. With the development of computer technology and numerical calculation, there are now many branches of topology optimization methods [12]. One of the most widely-used topology optimizations is the Solid Isotropic Material with Penalization (SIMP) approach [13,14]. The SIMP method has been widely deployed on many Computer Aided Engineering (CAE) systems, such as ANSYS, ABAQUS and so on. It is now generally known as the "density-based" approach and because of its versatility and expandability, the method is now applied in many fields, such as heat transfer, fluids, optics and acoustic [12]. However, the elimination of intermediate density elements has always been and is still an important topic in the density-based topology optimization method. Another method of topology optimization, the level set method, has the advantage of having clearly defined phases and geometrically smooth and clear boundaries. It was first proposed by Wang et al. [15] and the level set method has been extended for continuum structure by Allaire et al. [16] and Xia et al. [17,18]. Although the level set can provide a clear definition of the boundary, it is only captured in the physics when combining with a boundary conforming method such as the extended finite element method (X-FEM) [19]. Xie et al [20] proposed Evolutionary Structural Optimization (ESO) method, which avoids intermediate density elements using discrete updates based on intuitive stress limit condition. However, the ESO method has some difficulties with convergence and expandability, but these are, to some degree, reduced using the Bi-directional Evolutionary Structural Optimization (BESO) method [21]. With the development of recent topology optimization technology, it is widely used in mechanical structures, heat transfer and fluid problems amongst others [22].

Thermofluid topology optimization is an important branch of heat sink optimization because it provides a scheme for optimizing the temperature field as well as the fluid flow simultaneously, which affect the heat dissipation performance of heat sinks. However, thermofluid problems require the simulation of both the fluid flow and the heat transfer, coupling the fluid flow to the temperature field through convection. The computational cost of a single simulation may be an obstacle to optimization, requiring hundreds of simulations due to its iterative nature. In order to overcome that, many researchers have used Newton's law of cooling combined with a constant heat transfer coefficient to approximate the heat transfer to a fluid. Yin et al. [23] proposed a novel topology design scheme for electro-thermally actuated compliant mechanism. Another

approximate thermofluid model method is to use a surrogate model, that has been used by Iga et al. [24] and Joo et al. [25]. Bruns [26] investigated topology optimization of convection-dominated, steady-state heat transfer, proposing interpolating the convection boundary using density variations from element to element. This approach has been applied by [27] and [28] and was recently formalized in a continuous formulation using density-gradients by [29] and [30]. However, recent advances in computational power now allows for optimization of more complex problems. Therefore, many researchers are beginning to pursue an accurate solution to thermofluid topology optimization using full conjugate heat transfer models. Moreover, forced convection was initially investigated by [31] and [32] and has subsequently been extended by many authors, as is summarized in the review paper by [33]. Recently, turbulent fluid flow [34] and forced heat transfer [34] has been presented using a density-based topology optimization approach. Natural convection is less studied, with Alexandersen et al. [35] treating it for the first time using a 2D model. Subsequently, Alexandersen et al. [36] proposed a large scale fully parallel computational framework as a way to topology-optimize high-fidelity 3D heat sinks cooled by natural convection as well as passive cooling of light-emitting diode lamps [37]. In order to decrease the computational cost, Joo et al. [38] proposed a simplified model using Newton's law of cooling and correlations for the same problem. Furthermore, a simplified potential flow model has recently been proposed as a way to reduce computational cost at an acceptable accuracy [39,40].

Although topology optimization of 2D thermofluid models to some extent can predict the optimized shape for forced convection problems, it has inevitable error compared with full 3D thermofluid topology optimization. However, as pointed out above, this comes at a high computational cost and time. Therefore, many researchers are exploring simplified 2D approximations of the full 3D problems, giving a lower computational cost with acceptable accuracy. A pseudo-3D thermofluid model was first proposed by Haertel et al. [41] connecting a solid thermal base layer with a fluid-solid layer. In extension of this work, Zeng et al. [42] used a similar model to optimize a forced air heat sink with superior heat sink performance investigated through experimental and numerical investigation. Recently, Yan et al. [43] assumed a fourth-degree polynomial temperature profile of the heat sink thermal-fluid layer and a linear temperature profile in the substrate to do topology optimization at close to 2D computational cost with increased accuracy. All of the mentioned works about topology optimization of

thermofluid model are steady-state problems. Whereas, in view of the operating conditions of chip heat sinks, topology optimization of transient thermofluid is necessary, especially for treating the instantaneous behavior that requires to cool the chip as fast as possible. Therefore, a transient pseudo-3D thermofluid model is presented in this work. Inspired by that the work of Shevchuk et al. [44,45], an approximate analytical model is introduced in this study. The model provides an analytical expression based on a resistor and capacitor circuit to describe the transient heat sink temperature rise with respect to time, which was verified by experiment in [46].

This paper is organized as follows: the transient pseudo-3D forced convection heat sink model is developed in Section 2; the verification of reference model and pseudo-3D model is covered in Section 3, by comparing the pseudo-3D model with real 3D model for steady-state conditions; the overall topology optimization formulation is illustrated in Section 4 with implementation details; the superior performance of topology-optimized designs are verified through the comparison with a reference chip heat sink in Section 5, including comparison of transient optimized results, steady-state optimized results and a more practical model; finally, discussion and conclusions are provided in Section 6.

2. Transient pseudo-3D forced convection heat sink model

A schematic illustration of a full 3D chip heat sink model is shown in Fig. 1. The channel of the model is teemed with cooling medium and three heat sink slices are placed in the middle of the channel. At the bottom of the heat sink, there is a chip that generates heat. The heat of the chip is transferred mainly from the chip to the slices and then is taken away by the flowing cooling that flows in from inlet and flows out to the outlet. The simulation of full 3D model in this study is very costly. Thus, the pseudo-3D model is utilized in this study because it can be obtained by extruding from a 2D model.

As illustrated in Fig. 2, under the full 3D heat sink model is a “channel layer” defined as a cross-section through the full model. To demonstrate its pseudo 3D model more clearly, a pseudo 3D model structure sketch is displayed in Fig. 3.

As is shown in Fig. 3, the upper plane “channel layer” connects the temperature with flow fields. The layer includes the fluid which flows from inlet to the outlet. This layer

also contains the heat sink fin region in the fluid region. That transfers the heat from the base plate at the bottom to the cooling air. Thus, the shape of heat sink fin affects the flow paths of the cooling air and then greatly influence the heat dissipation performance of the heat sink.

The other region of the layer is a pure fluid region. Two non-slip boundaries are added at two longer edges of the model. Constant pressures are imposed on the inlet and the outlet of the channel. To simulate the chip reaching the turbo limit temperature and the start of the active cooling device, the temperature is set to 90℃, which is considered to be the turbo temperature limit for the i9-9900K chip in this study. The ambient temperature of the model is 25℃, which is also applied as the Dirichlet boundary on the inlet boundary. The lower layer is the “heat source layer”, which consists only of the heated base plate. With a uniformly constant heat production. All boundaries of this layer are adiabatic boundaries.

As described in Ref.[41], one part of the heat production is absorbed by the fins in the channel layer. The other part of heat production causes a rise of temperature of the base plate. The heat absorbed by the fins is much more easily taken away by the cooling medium than directly through the heat source, when the cooling air passes through the channel.

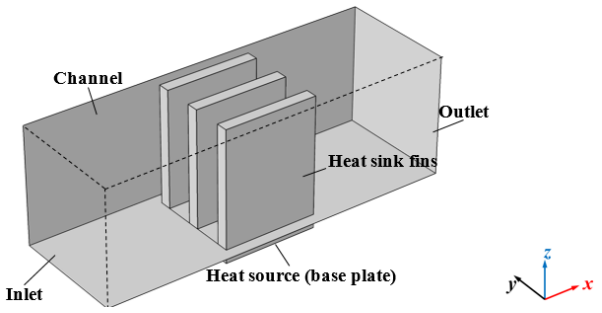

Fig. 1. Full 3D model of a reference straight-fin heat sink.

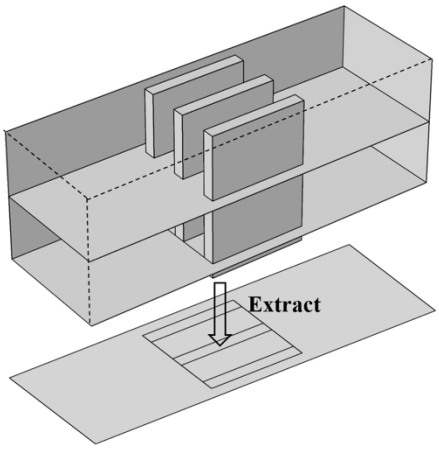

Fig. 2. Illustration of full 3D model and the corresponding solid-fluid "channel layer" of the pseudo-3D model.

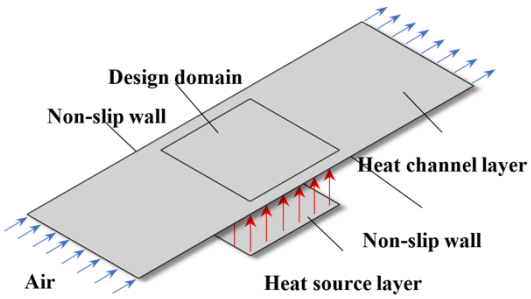

Fig. 3. Transient pseudo 3D model structure sketch

There are some assumptions are introduced in this model:

a) The flow field of the channel layer constitutes a laminar and incompressible flow;
b) The material properties of all phases are constant and do not change with temperature;
c) The fluid flow and the heat transfer are analyzed using a time-dependent solver since the instantaneous behavior is of interest.

2.1. Channel layer

Mathematical model of channel model

As the channel layer has two physical fields, flow field and temperature field, these two fields interact with each other. To establish an effective mathematical model for simulation, the Navier-Stokes equations of the channel layer are formulated as follow:

$$\frac{\partial \rho_f}{\partial t} + \nabla \cdot \left(\rho_f \mathbf{u} \right) = 0 \tag{1}$$

$$\rho_f \left(\frac{\partial \mathbf{u}}{\partial t} + \mathbf{u} \cdot \nabla \mathbf{u} \right) = -\nabla p + \mu \nabla^2 \mathbf{u} + \mathbf{f} \tag{2}$$

where **f** represents the source term of the fluid flow; ρ_f in Eqs. (1) and (2) denotes the fluid density; **u** is the velocity field of the model; p is the fluid pressure; and μ is the fluid viscosity. Due to the incompressible assumption and a constant density of the fluid, the mass conservation Eq. (1) changes as follows:

$$\nabla \cdot \mathbf{u} = 0 \tag{3}$$

When it comes to the heat transfer and the fluid flow, the energy conservation equation usually contains several terms representing different physical meanings, such as: heat diffusion term $k\nabla^2 T$; convection term $\rho_f c_f \mathbf{u} \cdot \nabla T$; temporal term $\rho_f c_f \partial T / \partial t$; and a source term f_c. Thus, synthesizing all differential terms above, the energy conservation equation is formulated as:

$$\rho_f c_f \frac{\partial T}{\partial t} + \rho_f c_f \mathbf{u} \cdot \nabla T - k\nabla^2 T = f_c \tag{4}$$

where c_f is the specific heat of the fluid and T denotes the temperature field of the model.

Boundary conditions of channel layer

As for the temperature boundary conditions of the channel layer, the fluid inlet temperature is set to the value of T_{in} =25℃, which can be expressed as:

$$T = T_{in} \quad \text{on} \quad \Gamma_{in} \tag{5}$$

where Γ_{in} represents the inlet boundary of the model. The temperature field boundary conditions for the outlet and walls in the channel layer are given by:

$$\mathbf{n} \cdot \nabla T = 0 \quad \text{on} \quad \Gamma_{out} \bigcup \Gamma_{wall} \tag{6}$$

The temperature of regions except the inlet boundary is set to a uniform value at the initial time, which means that the temperature of the chip starts at the turbo frequency temperature limit T_0 = 90ºC, and it is defined as:

$$T(\mathbf{x},t)\big|_{t=0} = T_0 \quad \mathbf{x} \in \Omega \ \bigcup \ \mathbf{x} \notin \Gamma_{in} \tag{7}$$

The velocity and the pressure boundary conditions of the channel layer are as follows:

$$\begin{cases} p = p_{in} & \text{on } \Gamma_{in} \\ p = p_{out} & \text{on } \Gamma_{out} \end{cases} \tag{8}$$

The magnitude of heat source term f_c of Eq. (4) consists of two parts. One part is transferred from the base plate to the channel layer through fins of the heat sink. The other part is from the cooling airflow that passes through the heat sink fins region in the channel layer. Therefore, the heat source term f_c is defined as:

$$f_c = \frac{h(T_b - T)}{t_{ch}} \tag{9}$$

$$h = \begin{cases} h_s, & \text{Solid phase} \\ h_f, & \text{Fluid phase} \end{cases} \tag{10}$$

where h is the convection coefficient, T_b is the base plate temperature field, and t_{ch} is the thickness of the channel layer.

2.2. Base plate layer

Mathematical model of base plate

The base plate is composed of the solid phase material, whose material property is constant. A constant heat production rate is imposed on the base plate. However, most of the heat is transferred to the channel layer. Thus, the differential equation denotes as follow:

$$\rho_s c_s \frac{\partial T_{bp}}{\partial t} - \nabla \cdot (k_s \nabla T_{bp}) = f_b \tag{11}$$

where ρ_s, c_s and k_s are the density, specific heat and thermal conductivity of the solid phase material and f_b is the heat source of the base plate, which can be expressed as:

$$f_b = \frac{Q}{V_{bp}} - \frac{q_{in}}{t_{bp}} \tag{12}$$

where Q represents the heat production power, V_{bp} is the volume of material of base plate, t_{bp} is the thickness of the base plate and q_{in} denotes the inner heat transferred between the channel layer and base plate layer, defined as:

$$q_{in} = h(T_{bp} - T) \tag{13}$$

Boundary conditions of base plate

The boundaries of the base plate are adiabatic, which is expressed as:

$$\mathbf{n} \cdot \nabla T_b = 0 \quad \text{on} \quad \partial\Omega_b \tag{14}$$

2.3. Determination of artificial heat convection coefficient h

The heat exchange in the full 3D model is mainly composed of the thermal convection on the interface between solid and fluid, and thermal conduction inside of the solid and fluid. The pseudo-3D model, however, only provides the heat transfer along with the layers without the heat conduction perpendicular to the layer. Therefore, the artificial

heat convection coefficient is introduced to probe the heat flux intensity between the two layers whose direction is vertical to the layer. Obviously, it will determine whether the pseudo-3D model could replace the full 3D model accurately during the simulation and optimization procedure. Haertel et al. choose the value of h intuitively in [41]. However, Zeng et al. provided detailed derivation processes in [42], which is used as a reference in this work.

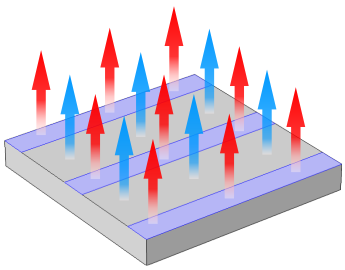

Fig. 4. Two main conduction paths of heat transfer from the heat source

The heat dissipation process of the 3D model shown in Fig. 1 contains two parts as shown in Fig. 4:

(1) Heat transferred to the air through the fins of the heat sink, shown as red arrows;

(2) Heat transferred directly to the air through the base plate exposed to the air, shown as blue arrows.

The two different areas have their heat dissipation capacity, which represents that they have different values of h. Therefore, it takes two limit values, representing the ability to dissipate heat in the solid denotes h_s and in the fluid denotes h_f.

For the fluid region, h_f reflects the heat convection ability of the base plate material with air. The definition is fully based on the numerical solution of the full 3D model in Fig. 1, and is given as:

$$h_f = \frac{q_{out}}{A_{wet}(T_{wet} - T_{air})} \tag{15}$$

$$q_{out} = \int_{\Gamma_{out}} \rho_f c_f u(T - T_{in}) d\Gamma \tag{16}$$

where q_{out} is the heat power brought out from the channel by cooling air at the outlet. A_{wet} and T_{wet} represent the area and average temperature of the surface of solid material contact with air, respectively. T_{air} in Eq. (15) is the average temperature of the air close to the solid surface.

The second part of the heat power is defined as follow:

$$q_{bp,d} = h_f A_{bp,wet}(T_{bp,wet} - T_{air,bp}) \tag{17}$$

where $A_{bp,wet}$ and $T_{bp,wet}$ are the area and the temperature of the surface of base plate exposed to cooling air, respectively. $T_{air,bp}$ represents the average temperature of the air close to the base plate. Therefore, the first part of heat dissipation power can be obtained by the difference between Q with $q_{bp,d}$:

$$q_{fin} = Q - q_{bp,d} = Q - h_f A_{bp,wet}(T_{bp,wet} - T_{air,bp}) \tag{18}$$

The heat conduction capacity from base plate to the heat sink fins is defined as:

$$h_s = \frac{q_{fin}}{A_{fin,bp}(T_{bp} - T_{fin})} \tag{19}$$

where $A_{fin,bp}$ is the area of region of base plate, with which the fins are contact, T_{bp} and T_{fin} are the average temperature of the base plate and fins, respectively.

3. Validation of reference and transient pseudo 3D model

A mesh dependency analysis of the reference design is made in Appendix A. It aims to verify the confidence of the reference FE model. Subsequently, the FE model is compared with the approximate resistor-capacitor (RC) model which is used to describe the temperature rise of transient heat sink.

3.1. Approximate RC model

In order to set up the approximate RC model, the following steps are used:

1) Principle of RC model

   An RC model was used to compare with experimental data of a transient heat sink by Zhou et al. [46]. In that work, the heat dissipation duration was divided into two periods: a transient period and a quasi-steady period. Because the period of focus in this paper is the initial transient period, only the transient heating duration is discussed here.

   The heat capacity C_h and resistance R of the heat sink play the role of the capacitance and resistance in the RC circuit. The temperature rise ΔT is regarded as the voltage rise in the circuit and the heat power Q is regarded as the electrical current intensity. Thus, the temperature rise can be described as:

$$\Delta T = QR(1 - e^{\frac{-t}{RC_h}}) \tag{20}$$

   If Q, C_h and R are known, the temperature rise of the chip can be acquired.

2) Implementation of RC model

The heat generation rate of the reference model Q is 4.3236W. The heat capacity of the model C_h is the heat capacity of the solid material of the model and is 0.41J/K here. The heat resistance is composed of conduction R_{cond} and convection R_{conv} resistance, which gives the total resistance:

$$R = R_{cond} + R_{conv} \tag{21}$$

R_{cond} is the heat resistance of the solid structure of the heat sink and can easily be obtained by:

$$R_{cond} = \frac{T_{avg} - T_c}{Q} \tag{22}$$

where T_{avg} is average temperature of the heat source, T_c is the temperature on the temperature condition boundaries and Q is the heat generation rate. The value of R_{cond} is 0.0398K/W. The convection resistance of the heat sink is determined by the heat sink structure and the flow velocity in the heat sink, and can be expressed as:

$$R_{conv} = \frac{1}{hA_{wet}} \tag{23}$$

where A_{wet} represents the surface area of the fins exposed to the air in the model, and h is the heat transfer coefficient between the solid material and coolant, which is determined from:

$$h = \frac{Q_{s\to f}}{A_{wet}(T_{wet} - T_{fluid})} \tag{24}$$

where $Q_{s\to f}$ is the transient heat power passing through the whole area exposed to the coolant, T_{wet} is the average temperature of surface exposed to the coolant and T_{fluid} represents the average temperature of the fluid (coolant) in the channel. Thus, the convection resistance can be expressed as:

$$R_{conv} = \frac{T_{wet} - T_{fluid}}{Q_{s\to f}} \tag{25}$$

All the values in the equation above can be found by the original simulation model. A fitted curve expression for R_{conv} with respect to time is given as:

$$R_{conv} = \begin{cases} (a_0 - a_3)/(1 + (t/a_2)^{a_1}) + a_3, & t \le 0.06\text{s} \\ 1.409 & 0.06\text{s} < t \le 1\text{s} \end{cases} \tag{26}$$

where a_0, a_1, a_2 and a_3 are equal to 990.5, 0.999, 2.068 and 1.206, respectively. Thereafter, the temperature rise of the heat source can be obtained by Eq. (20).

3) Comparison of the RC and reference model

The average chip temperature of the RC model is compared with the reference model shown in Fig. 5. The temperature rise has been calculated and compared with the temperature rise of the chip in 3D simulation model. It can be found that the overall trend of the temperature rise is very similar for the two models and the temperature rise in the reference simulation model fits the RC model well.

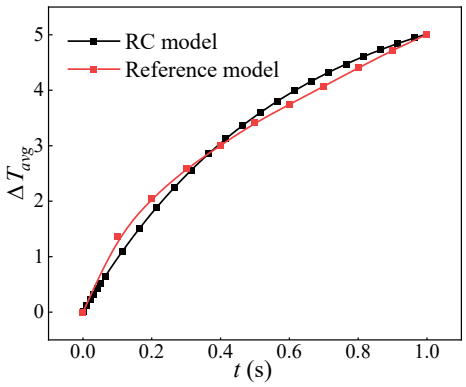

Fig. 5. Comparison of RC model with reference model

3.2. Validation of transient pseudo 3D model

Although the pseudo-3D model computationally costs lower than the full 3D model, it is an approximate model and its accuracy needs to be verified. The measure that is used to compare the two models is an average temperature criterion of the base plate:

$$f(t)=\begin{cases}\dfrac{1}{A_{bp}}\int_{\Omega_{bp}} T_{bp}-T_{in}d\Omega, & \text{for pseudo-3D}\\ \dfrac{1}{V_{bp}}\int_{\Omega_{bp}} T_{bp}-T_{in}d\Omega, & \text{for 3D}\end{cases} \tag{27}$$

The comparative benchmark is a 3D finite element (FE) model with three uniform heat sink slices inside of the heat sink channel. The temperature distribution of the base plate layer in the transient pseudo-3D model and the chip domain at the bottom of the channel will be used for comparison.

In the implementation of the transient pseudo-3D model, the differential equations of the overall model can be expressed as:

$$\begin{cases} \nabla \cdot \mathbf{u} = 0 \\ \rho_f \left(\dfrac{\partial \mathbf{u}}{\partial t} + \mathbf{u} \cdot \nabla \mathbf{u} \right) = -\nabla p + \mu \nabla^2 \mathbf{u} + \mathbf{f} \\ \rho_f c_f \dfrac{\partial T}{\partial t} + \rho_f c_f \mathbf{u} \cdot \nabla T - k \nabla^2 T = \dfrac{h(T_{bp} - T)}{t_{ch}} \\ \rho_s c_s \dfrac{\partial T_{bp}}{\partial t} - \nabla \cdot (k_s \nabla T_{bp}) = \dfrac{Q}{V_{bp}} - \dfrac{h(T_{bp} - T)}{t_{bp}} \end{cases} \tag{28}$$

The finite element analysis (FEA) procedure is implemented in COMSOL Multiphysics 5.4. The physical field variables in this model are composed of the velocity field **u**, pressure field p, temperature field of the channel layer T and temperature field of the base plate layer T_{bp}. The specific settings of the COMSOL Multiphysics are given in Appendix B.

The dimensions of the model are shown in Fig. 6. The parameters and material properties of the model are displayed in **Table 1** and **Table 2**. The values of $h_s = 9.8\times10^4$ W/(m^2·K) and $h_f = 90$ W/(m^2·K) are obtained by the calculation of the full 3D model according to Eqs. (15)-(19). Aluminum is chosen as the material of the solid phase of the model, with the material properties in **Table 2**. The inlet pressure of both models is set to 2Pa. Moreover, the mesh size ranges of pseudo 3D model and full 3D model are 0.3-0.45mm and 0.54-3mm, and their computation time are 32s and 1,585s, while on the same computer with Intel® Xeon™ E3-1230 V2 CPU and 16GB RAM. Obviously, just a single simulation procedure of pseudo-3D model can cut down much computational expense.

Table 1

Parameters of boundary conditions and model property of the pseudo 3D model and 3D model.

Parameters	Pseudo 3D model	3D model
T_{in} [°C]	25	25
t_{ch} [mm]	10	10
t_{bp} [mm]	1.15	1.15
Q [W]	4.3236	4.3236
p_{in} [Pa]	2	2
p_{out} [Pa]	0	0
h_s [W/(m²·K)]	9.8×10^4	—
h_f [W/m²·K]	400	—

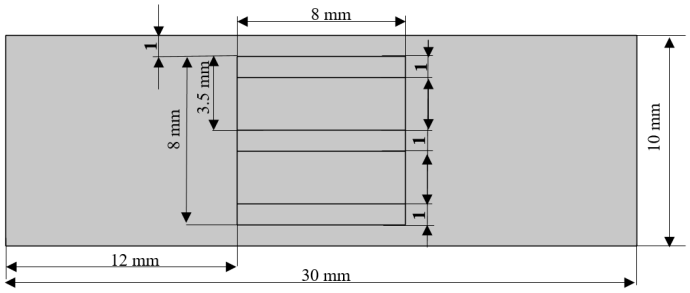

Fig. 6. Geometric sizes of transient pseudo 3D model

Table 2

Thermo-physical properties of pseudo 3D model and full 3D.

Thermo-physical properties	Values
k [W/(m·K)]	0.024
k_s [W/(m·K)]	237
ρ_f [kg/m^3]	1.204
ρ_s [kg/m^3]	2,700
c_f [J/(kg·K)]	1006
c_s [J/(kg·K)]	900
μ [Pa·s]	1.94×10^{-5}

With the FEA of transient pseudo-3D and full 3D model implemented in the software, the measure $f(t)$ is compared over time. To guarantee the accuracy of the transient process of heat dissipation, the mesh dependency analysis is demonstrated in Appendix A and a relatively long period time [0, 100]s is analyzed by the two models assuring that the field variables transit from transient to steady-state. As shown in Fig. 7, the measure of the two converge to nearly the same value, with only minor differences during the period time. That single indicator may not fully explain the equivalence of the two models, so the distribution of the temperature field of the base plate of the two models can help to explain its effectiveness and accuracy. To further describe their similarity in Fig. 8 quantitatively, a criterion g is introduced:

$$g = \frac{1}{A_{bp}} \int_{A_{bp}} \frac{\left| T_{3D} - T_{p3D} \right|}{T_{3D}} dA \tag{29}$$

where T_{3D} and T_{p3D} represent the temperature field of the base plate of the 3D and pseudo-3D models, respectively. The temperature field plane of the full 3D is the intermediate section of the chip located at the height of 0.575mm, which is the middle plane in the thickness direction (blue "z" axis shown in Fig. 1) of the chip.

In Fig. 8, it is obvious that there are some differences between the temperature profile of pseudo 3D and full 3D model. If the time-dependent h were used in the pseudo 3D

model, better agreement would be achieved. Besides, the simplification from 3D flow and temperature field to 2D leads to further differences. Thus, to obtain a much more accurate simulation result, the temperature profile should be further studied, and the boundary conditions of the model should be changed to maintain the flow uniformity in the direction of thickness. However, the accuracy study is not the core in this stage of work.

A value of $g = 2.462\times10^{-3} < 1\%$ is obtained from Eq. (29), which represents similar temperature fields between the two models.

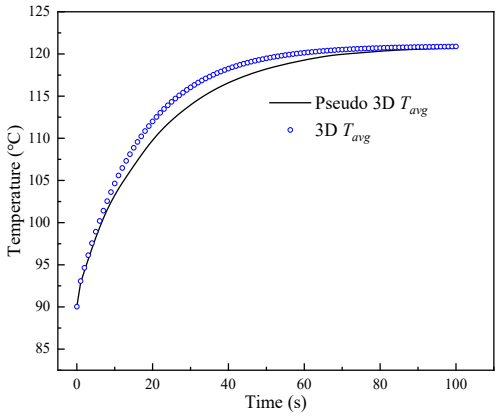

Fig. 7. Average temperatures of base plate of pseudo 3D and 3D models.

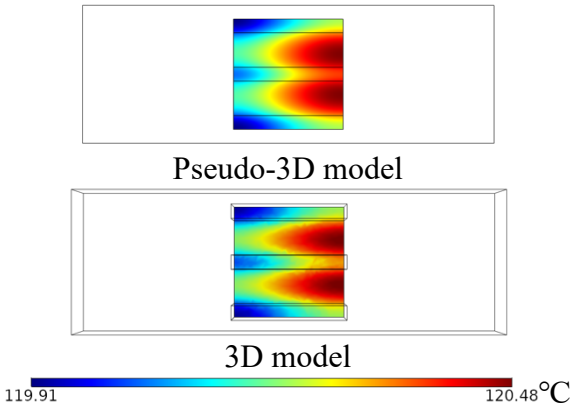

Fig. 8. Temperature distributions of the base plate of pseudo-3D and 3D models at 100s.

4. Topology optimization

4.1. Modified governing equations

The design variable θ is introduced in the design domain of the channel layer and varies in the range of (0, 1] and affects the material property of the model.

The Brinkman friction term is used in fluid flow topology optimization to penalize flow in the design domain and corresponds to the force exerted on a fluid flowing through an ideal porous medium in Ref. [47]. Thus, the Brinkman friction term is defined as:

$$\mathbf{f} = \alpha(\theta)\ \mathbf{u} \tag{30}$$

where $\alpha(\theta)$ represents the Brinkman friction coefficient and it can be expanded as:

$$\alpha(\theta) = \overline{\alpha} \cdot I_{\alpha}(\theta) = \frac{\mu}{DaL_c^{\,2}} \cdot I_{\alpha}(\theta) \tag{31}$$

where $I_{\alpha}(\theta)$ represents the interpolation function of the Brinkman friction coefficient as a function of the design variable. Da is the Darcy number of the fluid and L_c denotes the characteristic length of the model. In this work, Da is set to 1×10^{-5} and L_c is equal to $10mm$, which is also the height of the 3D channel.

In the energy conservation equation (4), there are several material properties including material density ρ, specific heat c, thermal conductivity k and convection coefficient h. As seen in Eq. (4) and Eq. (11), ρ and c always appear in the form of $\rho{\cdot}c$. To minimize the complexity of material interpolation for optimization, this product is considered as an independent material parameter $s = \rho{\cdot}c$ in the optimization procedure. Thus, the energy conservation equation can be modified as:

$$s(\theta)\frac{\partial T}{\partial t} + s(\theta)\mathbf{u}\cdot\nabla T - k(\theta)\nabla^2 T = \frac{h(\theta)(T_{bp} - T)}{t_{ch}} \tag{32}$$

where the expression of $s(\theta)$, $k(\theta)$ and $h(\theta)$ with respect to design variable θ denote:

$$\begin{cases} s(\theta) = s_f \cdot I_s(\theta) \\ k(\theta) = k_f \cdot I_k(\theta) \\ h(\theta) = h_f \cdot I_h(\theta) \end{cases} \tag{33}$$

As for the heat transfer equation for the base plate layer, Eq. (10), it is modified as:

$$\rho_s c_s \frac{\partial T_b}{\partial t} - \nabla \cdot (k_s \nabla T_{bp}) = \frac{Q}{V_{bp}} - \frac{h(\theta)(T_{bp} - T)}{t_{bp}} \tag{34}$$

4.2. Interpolation functions

A detailed analysis of the interpolation functions is introduced to study the variation of the chosen objective function with respect to design variable in this section, in order to obtain a better optimization behavior and better performing optimized design. This is because interpolation function affects the convergence to local optimum in the final design significantly, and the interpolation functions $I_j(\theta),\ j = \alpha, k, h, s$ are defined as:

$$I_j(\theta) = \begin{cases} \dfrac{1-\theta}{1+q_\alpha \theta}, & j = \alpha \\ \dfrac{\theta\left(C_j\left(1+q_j\right)-1\right)+1}{C_j\left(1+q_j\theta\right)}, & j = k, h, s \end{cases} \tag{35}$$

where q_α and q_j represent the penalty factors of inverse permeability and other three sorts of material properties. C_j is the ratio of the fluid and solid phase properties and denotes:

$$C_j = \begin{cases} \dfrac{k_f}{k_s}, & j = k \\ \dfrac{h_f}{h_s}, & j = h \\ \dfrac{s_f}{s_s}, & j = s \end{cases} \tag{36}$$

The shape of interpolation function I_s with different values of penalty factors is shown in Fig. 9. The four curves describe the effect of the convex factor q_s on the variation trend of interpolation function I_s. The figure illustrates that with the rise of q_s, the declination slope of interpolation function I_s increases. The above rule applies to other three interpolation function in this study.

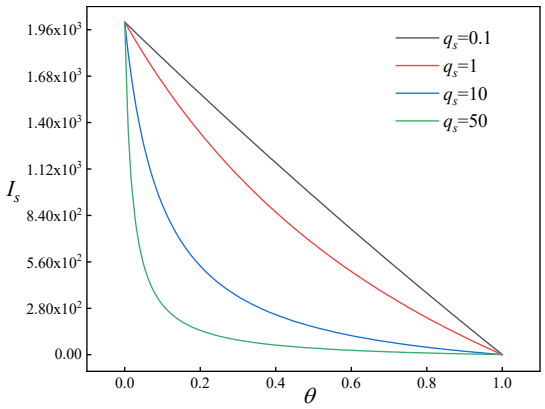

Fig. 9. Interpolation functions I_s of pseudo 3D model

4.3. Selection of the penalty factors

The model that is used to sensibly choose penalty factors is shown in Fig. 6 and the structure in the figure is chosen by intuition. However, the design does not affect the values of h_f, h_s and objective function significantly, and the representative design is sufficient for an initial choice[1].

Before the choice of penalty factors is made, the objective function is defined in order to measure the behavior of varying the penalty factors. The objective function is chosen as:

$$f(\theta) = \frac{1}{A_b}\int_{\Omega_{bp}} T_b - T_{in} d\Omega \Big|_{t=t_T} \tag{37}$$

where $f(\theta)$ is the relative average temperature of the base plate at the terminal time point. In this study, the terminal time is set to t_T =1s for observing transient heat dissipation period.

[1] A comparison has been made between the reference straight fin design and the "Initial design 4" introduced later in Fig. 13. The result shows a difference of h_f and h_s of those two models less than 5.56% and 1.47% respectively. In order to test the influence of h_f on base plate average temperature, simulations were performed for a range of h_f and show an error less than 0.1%.

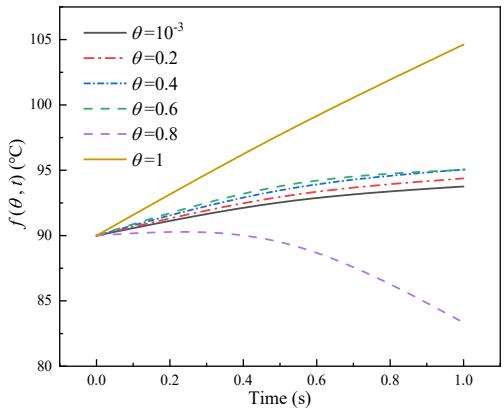

Fig. 10. Objective function varies with respect to time and different design variable values.

Figures of $f(\theta, t)$ with respect to time and different design variable values are shown in Fig. 10. The objective function generally increases with density value increasing, but at the value of 0.8 in the figure, the objective function curve is abnormal with a decrease in f over time. This indicates that unphysical behavior is obtained for intermediate design variables values. Thus, a study is implemented to describe the relationship between the objective function $f(\theta)$ in Eq. (37) and design variable θ.

Similarly to the studies published by [48] and [49], the objective function is shown in Fig. 11 for many sets of penalty factors for varying design variable θ. An intuitive rule can be obtained from the 27 subgraphs with 108 curves in Fig. 11: each penalty factor value particularly takes effect on the position of the minimum point of the curve.

The objective function $f(\theta)$ should be a monotonously increasing curve from $\theta = 0$ (being fully solid fins) to $\theta = 1$ (being no fins or fully fluid). This ensures that the minima with respect to the single variable is at the case of $\theta = 1$ and a smooth transition from one value to another, without any local minima with respect to the single variable. The observed trends are as follows:

a) With an increase of the value of q_α, the position of the minimum point moves left and downward;

b) With an increase of the value of q_k, the position of the minimum point moves left and downward;

c) With an increase of the value of q_h, the position of the minimum point moves left and up;

d) With an increase of the value of q_s, the position of the minimum point moves right and up.

Based on their particular influences on the position of the minimum point, the well-performed penalty factors value can be easily determined. Therefore, the values of the penalty factors chosen in this study are q_α =0.1, q_k =0.1, q_h =50 and q_s =100, respectively. Thus, the curve of those penalty factors in Fig. 12 shows a monotonically increasing trend, which denotes that they are feasible in this study. Their performance in topology optimization could be verified in Section 5.

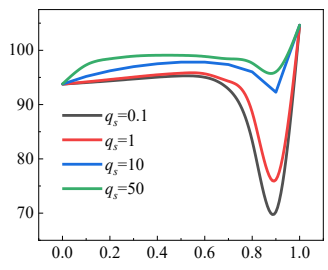

q_α =0.1, q_k =0.1, q_h =0.1

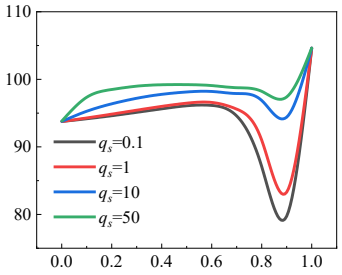

q_α =0.1, q_k =0.1, q_h =1

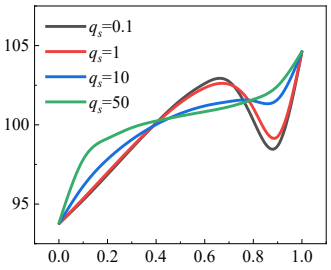

q_α =0.1, q_k =0.1, q_h =10

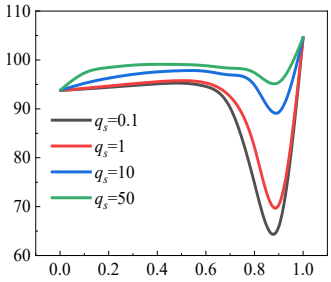

q_α =0.1, q_k =1, q_h =0.1

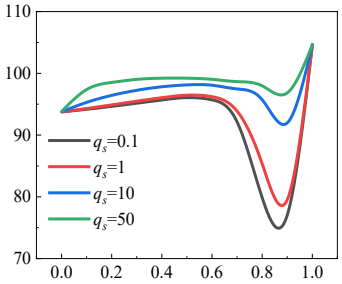

q_α =0.1, q_k =1, q_h =1

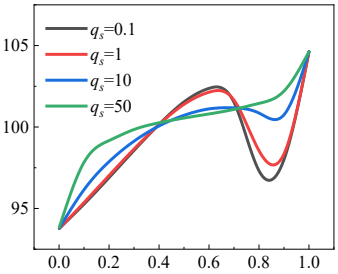

q_α =0.1, q_k =1, q_h =10

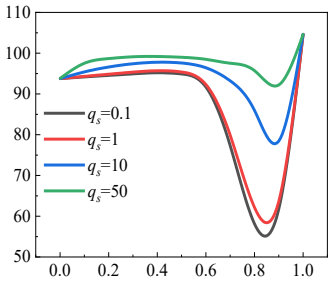

q_α =0.1, q_k =10, q_h =0.1

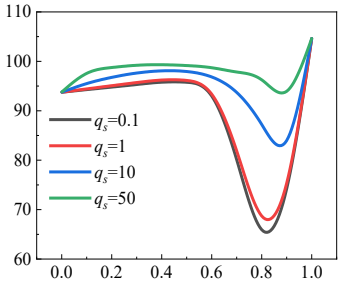

q_α =0.1, q_k =10, q_h =1

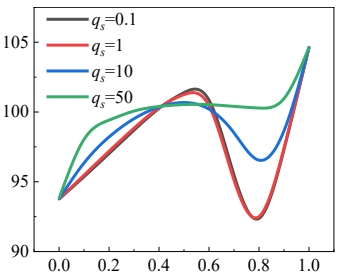

q_α =0.1, q_k =10, q_h =10

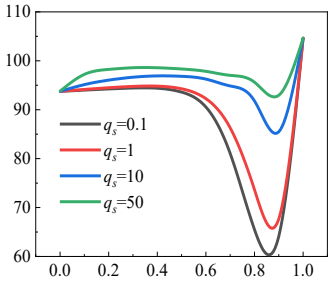

q_α =1, q_k =0.1, q_h =0.1

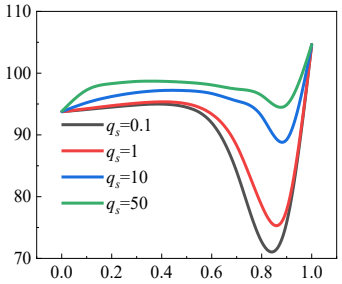

q_α =1, q_k =0.1, q_h =1

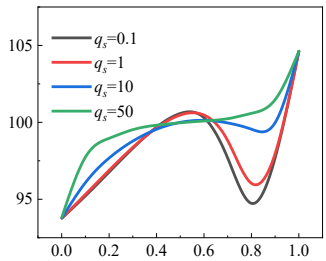

q_α =1, q_k =0.1, q_h =10

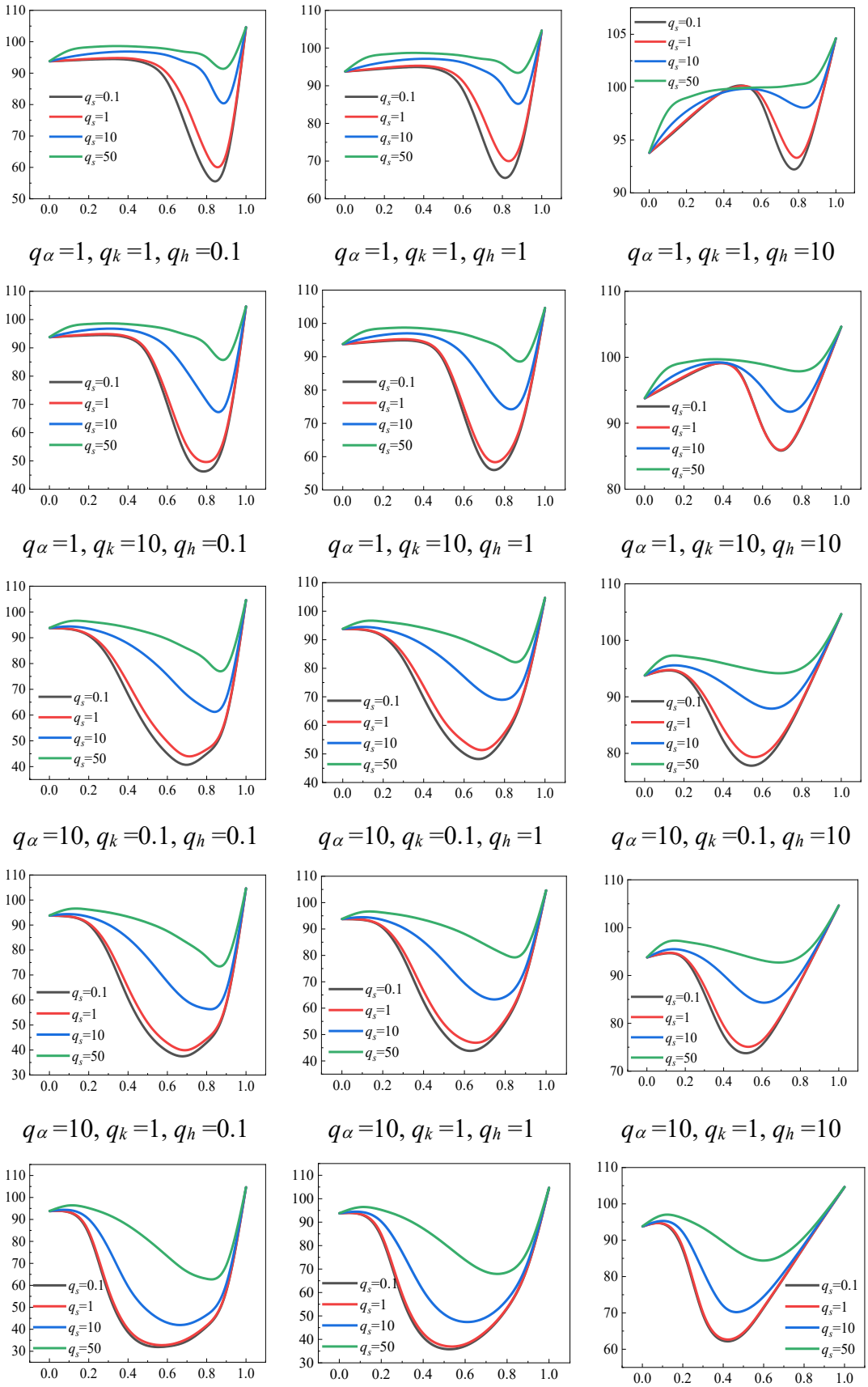

q_α =1, q_k =1, q_h =0.1 q_α =1, q_k =1, q_h =1 q_α =1, q_k =1, q_h =10

q_α =1, q_k =10, q_h =0.1 q_α =1, q_k =10, q_h =1 q_α =1, q_k =10, q_h =10

q_α =10, q_k =0.1, q_h =0.1 q_α =10, q_k =0.1, q_h =1 q_α =10, q_k =0.1, q_h =10

q_α =10, q_k =1, q_h =0.1 q_α =10, q_k =1, q_h =1 q_α =10, q_k =1, q_h =10

q_α =10, q_k =10, q_h =0.1 q_α =10, q_k =10, q_h =1 q_α =10, q_k =10, q_h =10

Fig. 11. 27 subgraphs with 108 curves of objective function varies with respect to

design variable with 108 kinds of penalty factor combinations.

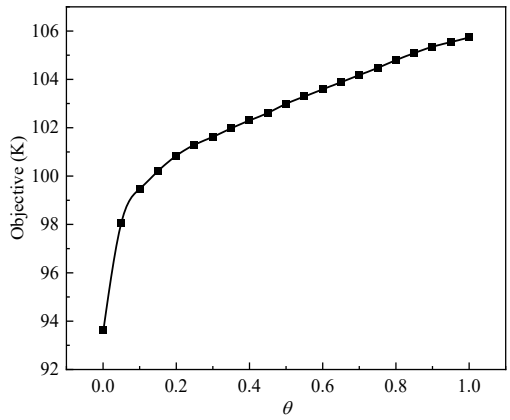

Fig. 12. Objective function varies with respect to the design variable with penalty factors q_α =0.1, q_k =0.1, q_h =50, q_s =100.

4.4. Implementation of topology optimization

In this work, the optimization problem is handled as a constrained minimization problem:

$$\begin{aligned} \min_{\theta}: \quad & f(\psi(\theta,t),\theta,t) \\ \text{s.t.}: \quad & \gamma(\psi(\theta,t),\theta,t)=0 \\ & \iint_{\Omega_d}(1-\theta)dxdy - f_V A_{\Omega_d} \le 0 \\ & 0<\theta(\mathbf{x},t)\le 1 \quad \forall \mathbf{x}\in \Omega_d, t\in[0,t_T] \end{aligned} \tag{38}$$

where $\psi(\theta,t)$ represents the field variable vector including the temperature field, velocity field and pressure field; $\gamma(\psi(\theta,t),\theta,t)$ denotes the residual of the finite element formulation of the full thermofluid problem; Ω_d and A_{Ω_d} are the design domain and area of the design domain, respectively; f_V is the volume fraction of the constraint set in this model; and **x** denotes the spatial coordination vector of the model. During the process of topology optimization, design filtering is necessary in the transient thermofluid model to avoid checkerboard problems [50]. A partial differential equation (PDE) filter is used in the topology optimization procedure, which defined as:

$$-r_{fil}^2\nabla^2\tilde{\theta}+\tilde{\theta}=\theta \quad \text{in } \Omega_d \tag{39}$$

where r_{fil} and $\tilde{\theta}$ represent the filter parameter and filtered design variable, respectively. Because the surroundings are fluid domain, the boundary conditions of the filter PDE

can be expressed as follows:

$$\tilde{\theta} = 1 \text{ on } \partial\Omega_d \tag{40}$$

To further reduce the intermediate density elements on the interface between solid and fluid the design domain, a smoothed Heaviside projection is applied on the filtered design field:

$$\bar{\tilde{\theta}} = \frac{\tanh(\beta\eta) + \tanh\left(\beta\left(\tilde{\theta} - \eta\right)\right)}{\tanh(\beta\eta) + \tanh(\beta(1-\eta))} \tag{41}$$

where $\bar{\tilde{\theta}}$ denotes the projected design field, β is a parameter controlling the slope of the projection function, and η is the projection threshold parameter. The projected design field $\bar{\tilde{\theta}}$ is substituted with the initial design field in the modified governing Eqs. (28), (30) and (32), and the interpolation functions (33). Sensitivities are subsequently corrected using the chain rule.

Topology optimization of the transient pseudo-3D model is implemented in the commercial FEA software COMSOL Multiphysics [51]. The governing equations (28) and (30) are calculated in the "Heat transfer in solids and fluids" module, coupling with the "Laminar flow" module to obtain the temperature field *T*, the velocity field **u** and pressure field *p*. Eq. (32) is implemented in a heat partial differential equation to obtain the temperature field of the base plate T_{bp}. The coupled models are solved using the time-dependent FE solver. The optimization method used in this model is GCMMA, with the number of inner iteration per outer step is set to 1. The specific settings of COMSOL Multiphysics are detailed in Appendix B.

5. Results and discussion

Due to the highly non-linear and non-convex properties of the optimization problem, the optimizer will always converge to a local optimal structure. One method to alleviate this problem is choosing different initial designs of the model. Then, the optimized results are compared with the corresponding full 3D model to validate their transient performance. Furthermore, steady-state optimized results are also compared to highlight the characteristics of the transient model. Lastly, a practical model is built with more powerful cooling medium and higher inlet pressure.

5.1. Initial design

In this section, several initial designs are proposed and then an overall comparison is made to select a better initial design for the topology optimization. Four different initial design layouts are shown in Fig. 13. The first represents a uniform design field (θ_0 =0.8) in the design domain and the other figures are three solid cylinders in different positions of the design domain. It is necessary to figure out which initial design has a relatively better convergence result. The input pressure for the topology optimization procedure is set to 1Pa rather than 2Pa, because the transient solver cannot converge under the prescribed tolerance during optimization in the software. As the inlet condition changes, the heat exchange coefficient correspondingly changes to h_s=6.5×10^{4}W/(m^2·K) and h_f=90W/(m^2·K). The other optimization parameters are shown in **Table 3**. n_{ev} represents the number of model evaluations and the tolerance of optimization ε controls the optimization convergence. d_{min} and r_{min} refer to the minimum mesh size and filter radius of the model, respectively. f_V is the volume fraction constraint. q_α, q_k, q_h and q_s are the penalty factors with respect to inverse permeability, thermal conductivity, heat convection coefficient and product of density and specific heat of the design domain material respectively. β and η are the projection steepness parameter and threshold parameter in Eq. (34).

The choice of 4 initial designs in Fig. 13 relies on several reasons: Firstly, the comparison of uniform and non-uniform density distribution need to be made; Secondly, because the design domain and the model is axisymmetric, the density layouts selected in this section are axisymmetric as well; Lastly, the layout of rounds that represent cylinder heat sink fins in full 3D model, in Initial design 2-4 refers to the layout of initial designs of *model a* in [52] to compare the performance of different layout directions and fins number.

The mesh of the pseudo 3D topology optimization is shown in Fig. 14. Symmetry is adopted in the optimization process in order to reduce computational effort.

After optimization, four initial designs converge to the optimized structures shown in Fig. 16, whose physical fields are shown in Fig. 17, Fig. 18 and Fig. 19. The objective convergence curves are shown in Fig. 15 and performance measures of the 4 optimized designs and a reference are shown in Fig. 20. Only the optimized 1, 2, and 4 and two regular heat sinks are displayed in the figure because the performance curve of 3th

optimized is too similar to the 2th to separate them. Besides, the "V" displayed in Fig. 20 represents the total volume of the design domain with a value of 640mm^3.

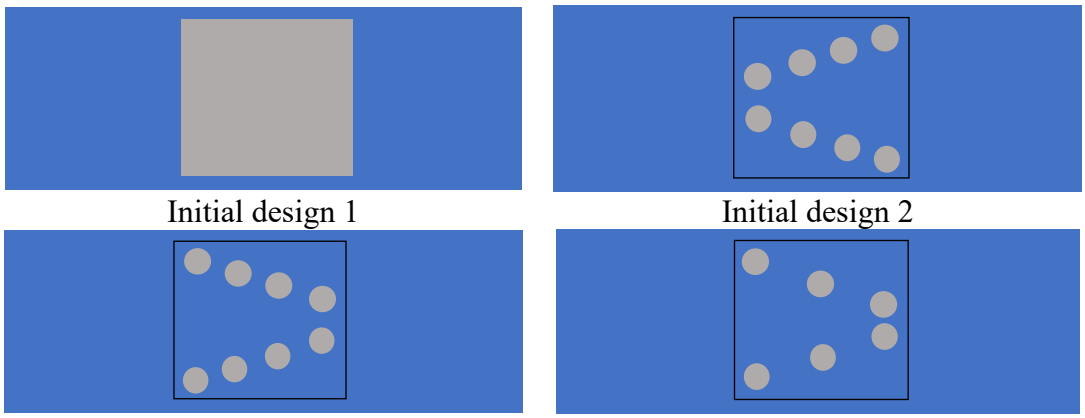

Fig. 13. Four different initial designs of the pseudo 3D topology model.

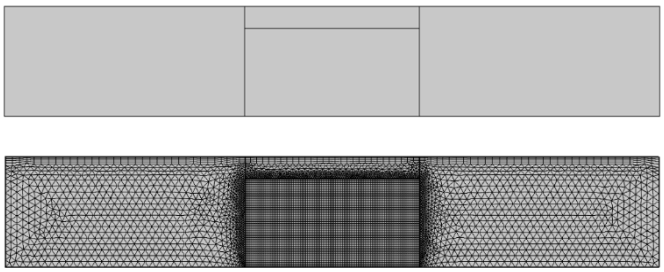

Fig. 14. The sketch of topology optimization model and the mesh.

Table 3

Parameters of optimization process.

Parameters of optimization	Values	Parameters of optimization	Values
Da	1×10^{-6}	q_α	0.1
n_{ev}	300	q_k	0.1
ε	1×10^{-3}	q_h	50
d_{min} $[mm]$	0.133	q_s	100
r_{min} $[mm]$	0.2	β	8
f_v	0.5	η	0.5

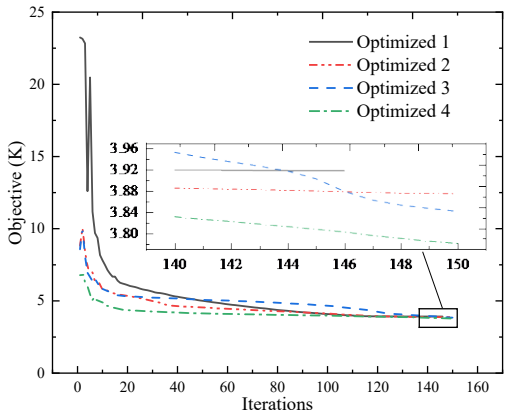

Fig. 15. Objective function with respect to the iteration numbers of initial designs 1, 2, 3 and 4.

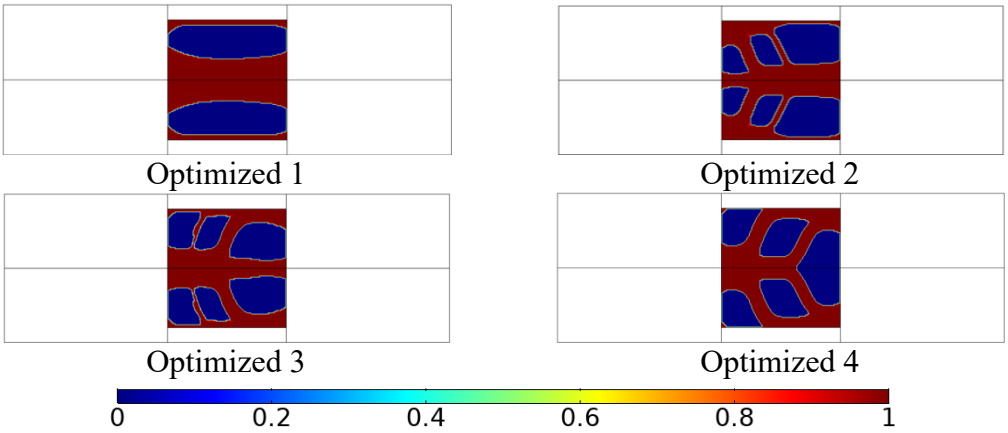

Fig. 16. Four optimized structures obtained from four different initial designs.

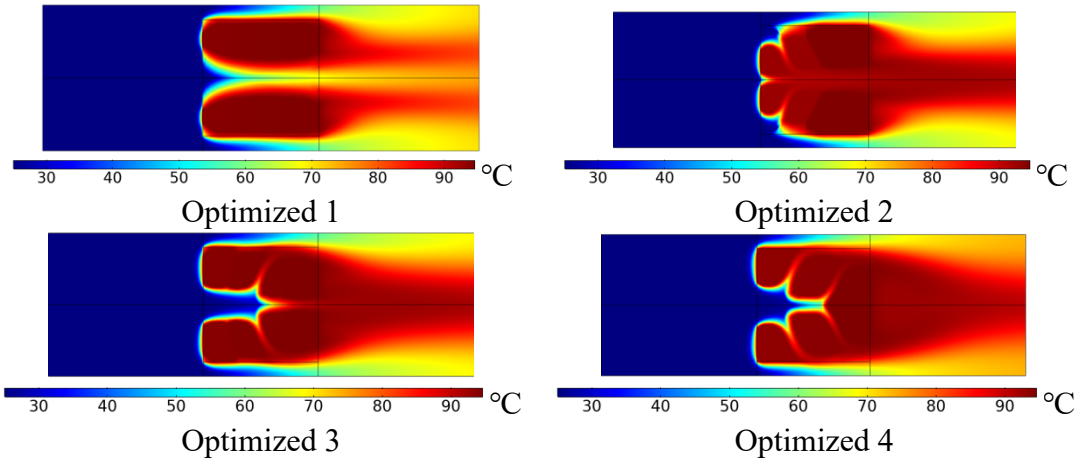

Fig. 17. Temperature distribution of the channel layer for the 4 optimized structure.

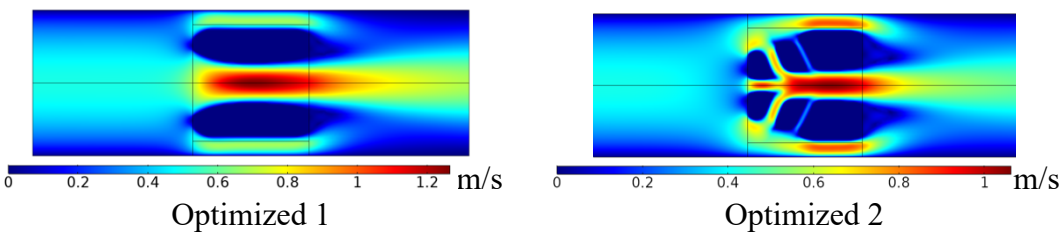

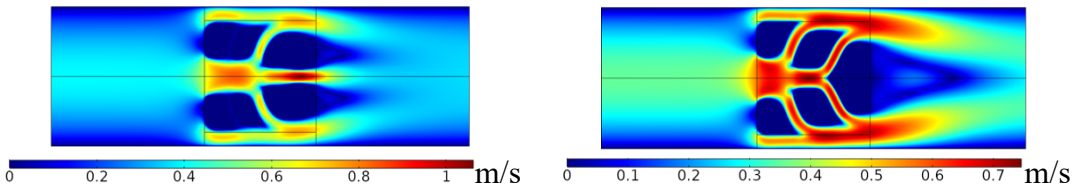

Optimized 3 Optimized 4

Fig. 18. Velocity distribution of the channel layer for the 4 optimized structure.

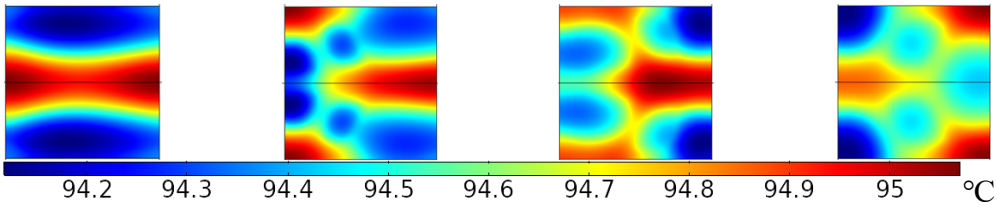

Optimized 1 Optimized 2 Optimized 3 Optimized 4

Fig. 19. Temperature distribution of the base plate layer for the 4 optimized structure.

According to Fig. 15, the 4th initial design produces the best performing design with minimal average base plate temperature. In Fig. 16, it can be found that the fluid channels through the design are generally thicker than for the other designs. This corresponds to higher fluid velocities through the heat sink geometry in Fig. 18. This translates to overall higher heat dissipation through convection and a better cooling of the base plate layer. It is interesting to note that in Fig. 17, the 2nd initial design has lower temperatures in the foremost fins than the other designs. This only translates to lower local base plate temperatures in Fig. 19, but as seen from Fig. 15, a slightly higher average base plate temperature than the 4th initial design.

Furthermore, the design layout is determined by the utility of Brinkman penalization, in which the physical field boundaries are not as clear as for a pure fluid and solid structure. By setting a threshold of the design field at a predefined value of 0.8, this allows for extrusion of the design to 3D for verification.

For comparing the pseudo-3D and full 3D models, we chose two performance measures:

a) The average temperature T_{avg} of the heat source;

b) The pumping power P_{pump} required to cool heat sink.

The consuming pumping power of the heat sink is defined as follows:

$$P_{pump} = r_f \cdot p_{drop} \tag{42}$$

where r_f represents the volumetric flow rate passing through inlet and p_{drop} is the pressure drop of the overall heat sink. The volumetric flow rate r_f is formulated as:

$$r_f = v_{in} A_{in} \tag{43}$$

Lastly, the velocity at the inlet $v_{in}|_{t=1s}$ and the heat sink volume V_{hs} are important to compare the various designs.

Table 4

Performance measures of 4 different optimized result in Fig. 19 and reference structures.

Structure	$V[mm^3]$	$T_{avg}|_{t=1s}$ [°C]	$v_{in}|_{t=1s}$ [°C]	A_{wet} $[mm^2]$	$P_{pump}|_{t=1s}$ [mW]
Ref.(0.375V)	240	94.97	0.369	540	0.0369
Optimized 1	320	94.72	0.524	403.58	0.0524
Optimized 2	320	94.54	0.315	607.65	0.0315
Optimized 3	320	94.53	0.314	594.33	0.0314
Optimized 4	320	94.24	0.242	541.09	0.0242
Ref.(0.5V)	320	94.38	0.257	560	0.0257

It can be seen from Table 4, that the best performing design is “optimized 4”, which is optimized starting from initial design 4. Two reference designs are introduced for the comparison, both of them are straight fin heat sinks but with two different material volume fractions (of the design domain volume), namely 0.375V and 0.5V. The 0.375V design is introduced because it has the same wetted area as the best optimized design. The 0.5V reference design is introduced because it has the same material volume as the optimized designs. With the same wetted area, the average temperature of the heat source at 1s of the Optimized 4 design is 0.721°C lower than that of the reference (0.375V). In terms of pumping power, the optimized 4 design decreases the pumping power by 34.3% of that for the reference design (0.375V). This indicates that the optimized design only uses 65.7% of the pumping power and reduced the volume average temperature of the chip by 0.721°C at t=1s, both compared to the reference design. Using the same material volume, compared to the reference heat sink (0.5V), the Optimized 4 heat sink decrease only 0.14°C of temperature and 5.1% of pumping power.

From the data in **Table 4**, it can be seen that having more wetted area is not necessarily a benefit when it comes to cooling performance. The best performing design (Optimized 4) has the third lowest wetted area, but the best thermal performance. The reference design (0.375V) has the same wetted area, but the thermal performance is worse, and the pumping power is significantly higher. The other reference design (0.5V)

has the same material volume and slightly higher wetted area, but worse thermal performance as well. Therefore, it is clear that it is not a simple question of the amount of heat sink area or heat sink volume. It is very important how to distribute the material and surface area, which is topology optimization introduces a significant advantage for heat sink design. These observations are perfectly in line with what has previously been observed for topology-optimized designs of passive heat sinks for light-emitting diode lamps in Ref. [37,53].

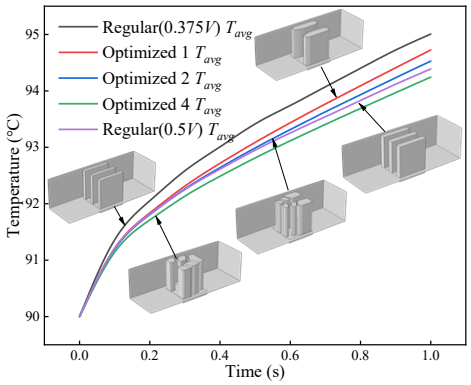

Fig. 20. Average temperature of chip of different structures

5.2. Comparison with steady-state pseudo 3D topology optimization model

To highlight the importance of using a transient model for treating the instantaneous behavior, the transient pseudo-3D model is compared to a steady-state pseudo-3D model. The comparison is divided into two parts:

a) The superior steady-state heat dissipation performance of the steady-state optimized structure compared to the reference design;
b) The superior instantaneous thermal performance of the transient optimized structure compared to the steady-state optimized structure.

To make it comparative, the initial design of the steady-state optimization is the same as the Initial design 4 in Fig. 13, which performs best out of the four different initial designs for the transient case. After the topology optimization, the physical fields of the optimized structure are shown in Fig. 21. Compared with transient model, steady-state optimized structure tends to have more sharp features and relatively less solid material volume. This is likely because for optimal steady-state performance, an aerodynamic design with low flow resistance is necessary. But for optimal instantaneous performance,

other phenomena are dominant due to the heat capacity of the design.

The mesh of the steady-state pseudo 3D model is the same as that of the transient model as shown in Fig. 14. The constraint that represents the volume fraction of the entire design domain of the optimization is set to f_v=0.5. The objective function of the optimization is set to the average temperature of the chip when it reaches steady state. The boundaries of solid and fluid phase chosen for the thresholded surface is a design variable of 0.8 too. Therefore, according to the thresholded boundaries, the geometry is extruded to the 3D model to verify its thermal performance.

As illustrated in Fig. 22 and Fig. 23, the steady-state average chip temperature of the steady-state optimized structure is about 20℃ lower than that of the reference design. This may be because steady state design has much sharper features and more fins than the reference one. This validates the superior steady-state thermal performance of the design generated by topology optimization.

For comparison, the transient performance of the steady-state design is now compared to the transient pseudo-3D topology optimization model. The average temperature performances are displayed in Fig. 24 and Fig. 25, for the time periods [0, 1s] and [0, 200s], respectively. As can be seen in Fig. 24, the instantaneous thermal performance of the transient pseudo-3D model is better than that of steady-state pseudo 3D model during the period of [0, 8]s. However, as time goes on over 8 seconds, the steady-state design becomes the better performer. This clearly shows that if the instantaneous transient response is of importance, steady-state analysis is not good enough on the condition in this section.

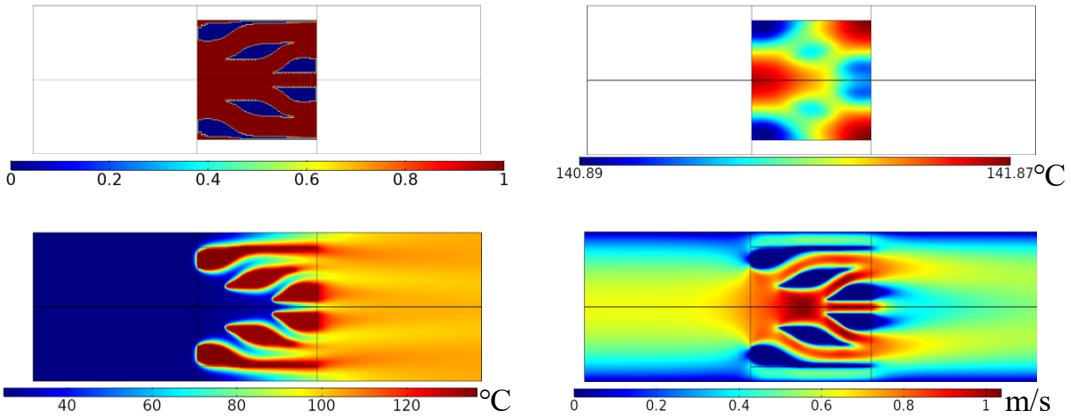

Fig. 21. Design variable layout, base plate temperature, channel temperature and channel velocity of steady-state topology optimized pseudo 3D model.

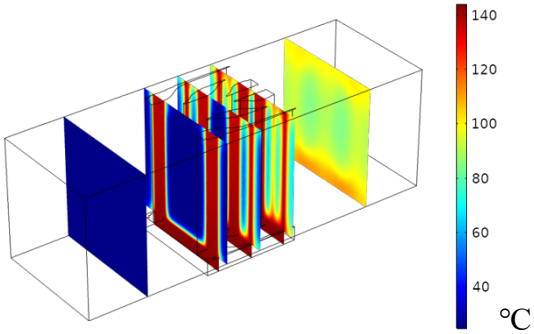

Fig. 22. Temperature layout of optimized steady-state 3D model.

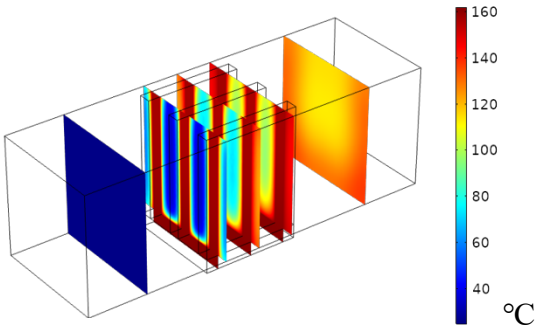

Fig. 23. Temperature layout of reference 3D model.

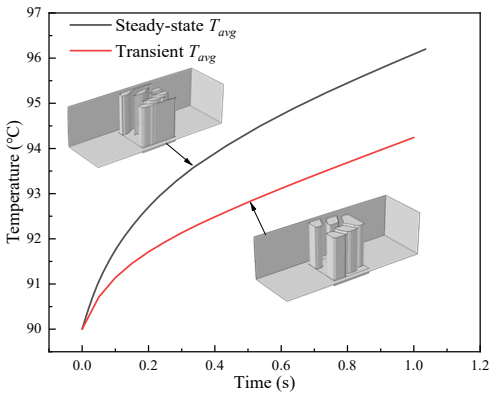

Fig. 24. The average temperature of optimized steady-state 3D model and optimized transient 3D model during [0, 1s].

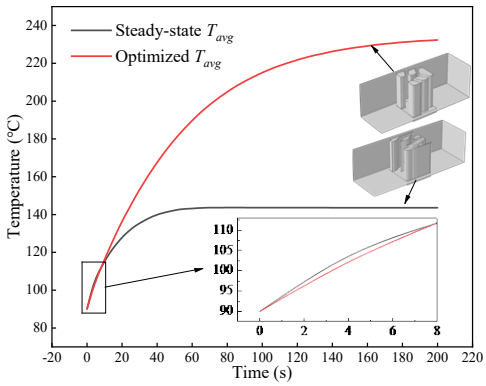

Fig. 25. The average temperature of optimized steady-state 3D model and optimized transient 3D model during [0, 200*s*].

5.3. A practical problem

In this section, to apply the proposed model to a more practical situation, a more powerful cooling medium and more realistic pressure input than the previous model are adopted in this section. Thus, water is chosen as the cooling medium to replace air and the pressure input rises to 50Pa. A shorter terminal time $t_T = 0.1$s is chosen in this model because of shorter transient period. The solid phase of the model is still aluminum.

The length of the channel is reduced to 12mm, which aims to reduce the degrees-of-freedom of the non-design domain in order to cut down the calculation time and allow a finer mesh in the design domain. The 3D model and its corresponding pseudo-3D model are shown in Fig. 26.

As the material properties and the boundary condition change, the heat transfer coefficients h_s and h_f are updated too. The transient 3D model shown in Fig. 1 is use to obtain the value of h_s and h_f, according to the Eqs. (15)-(19). Therefore, the value of material properties and heat transfer coefficients are displayed in **Table 5** and **Table 6**. The temperature profiles of the base plate for the pseudo-3D and full 3D models are demonstrated in Fig. 27. The similarity criterion g in Expression (29) is used to compare the temperature profiles, with a value of $g = 5.62\times10^{-3}$ showing a high similarity of the base plate temperature profile for the two models.

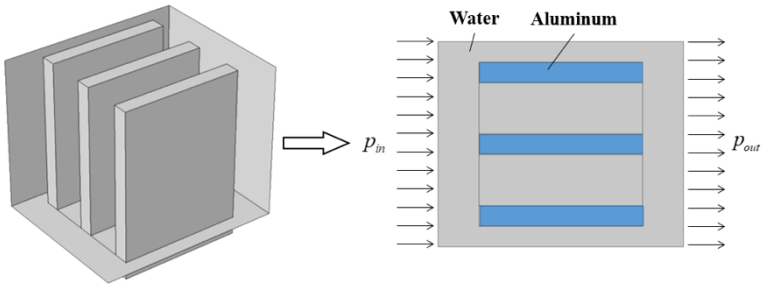

Fig. 26. Geometric diagram of 3D model and the corresponding pseudo-3D model.

Table 5

Parameters of boundary conditions and model property of pseudo 3D model and 3D model.

Parameters	Pseudo 3D model	3D model
T_{in} [°C]	25	25
t_{ch} [mm]	10	10
t_{bp} [mm]	1.15	1.15
Q [W]	50	50
p_{in} [Pa]	50	50

p_{out} [Pa]	0	0
h_s [W/(m^2·K)]	2×10^5	—
h_f [W/m^2·K]	5×10^3	—

Table 6

Thermo-physical properties of pseudo 3D model.

Thermo-physical properties	Values
k [W/(m·K)]	0.6
k_s [W/(m·K)]	237
ρ_f [kg/m^3]	988
ρ_s [kg/m^3]	2,700
c_f [J/(kg·K)]	4,185
c_s [J/(kg·K)]	900
μ [Pa·s]	8.94×10^{-4}

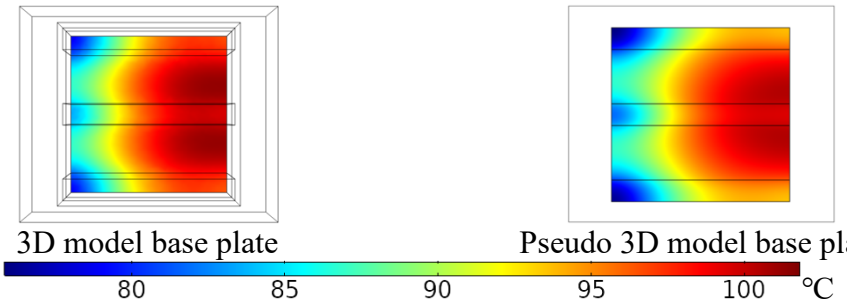

Fig. 27. The temperature profiles of base plate of pseudo 3D model and 3D model.

Besides, the penalty factors q_α =0.1, q_k =0.1, q_h =0.1 and q_h =100 are chosen, according to the intuitive rule proposed in Section 4. The objective function curve with respect to design variable θ is shown in Fig. 28. A monotonously increasing curve should yield a relatively low proportion of intermediate design variables in the final topology optimization result.

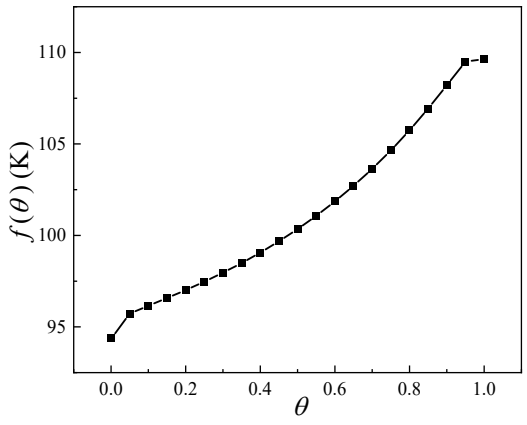

Fig. 28. Objective function curve with respect to design variable.

The sketch and mesh of the model are shown in Fig. 29, in which a very fine quadrilateral mesh is used, as well as boundary layer regions. The reason for applying a structured meshes in the case is to keep the accuracy of the calculation and reduce the computation cost. The discretized model has 10050 quadrilateral elements with 66524 of degree of freedom. The detailed analysis of replacing the unstructured mesh with a structured one are demonstrated in Appendix A. Fig. 30 shows the best performing initial design variable layout from Section 5.1, which is also used in this model.

The other optimization configurations are the same as the optimization procedure in Section 5.1. Fig. 31 shows the optimization process of 140 iterations. The design variable converges to a layout shown in Fig. 32, along with the channel temperature, channel velocity and base plate temperature fields.

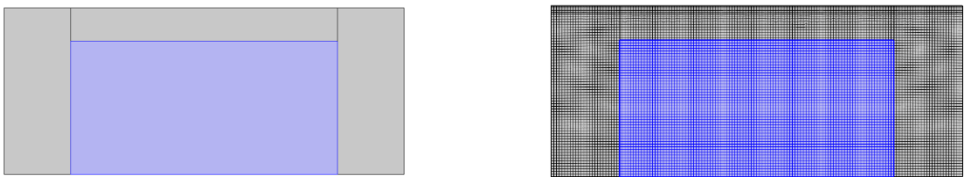

Fig. 29. The sketch of topology optimization model and its meshes.

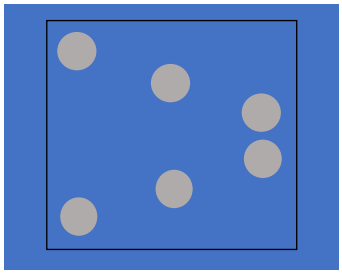

Fig. 30. Initial design of the pseudo 3D topology optimization model.

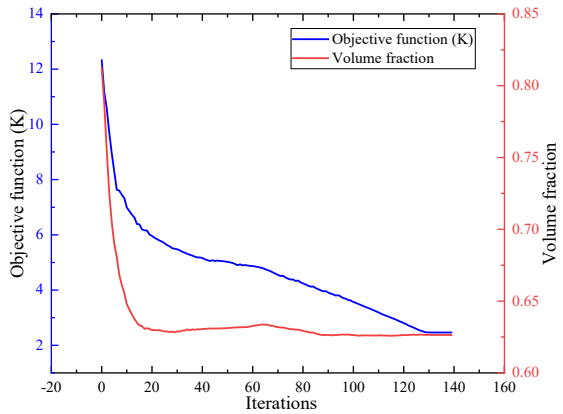

Fig. 31. Objective function and volume fraction of transient topology optimization pseudo 3D model with respect to iteration number.

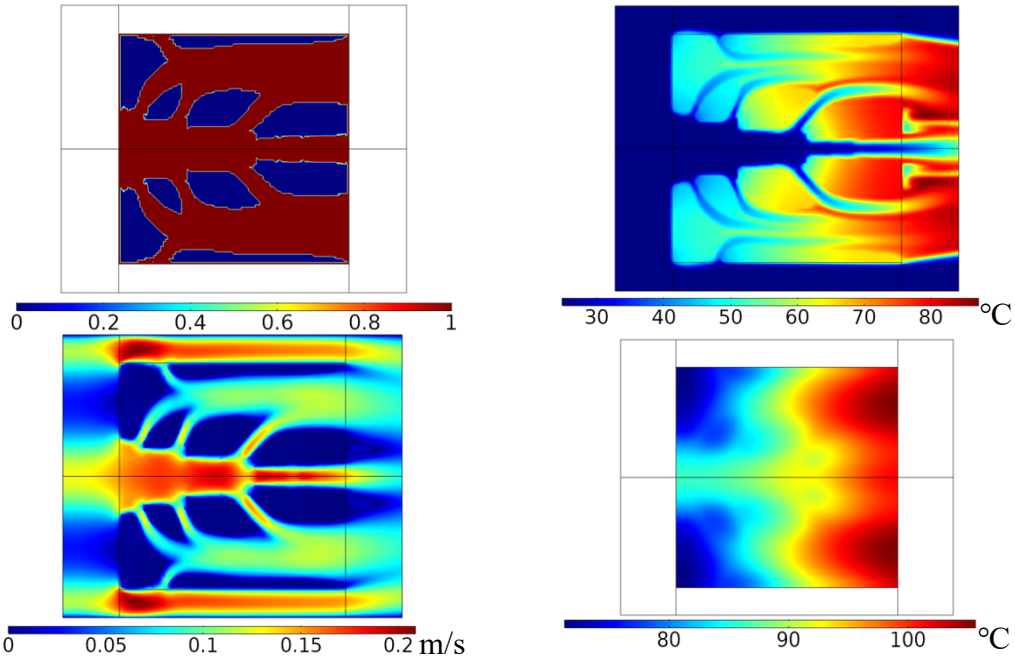

Fig. 32. Design variable layout, channel temperature, channel velocity and base plate temperature of the topology optimized pseudo 3D model.

Instantaneous comparison

Since the converged volume fraction is 0.625 in Fig. 31, the stretching model has the same solid material consumption as the reference model in Fig. 26. Therefore, comparisons in terms of average base plate temperature and pumping power with the reference heat sink are made during a period of 0 and 0.1s. This can be seen in Fig. 33 and Fig. 34, where it is obvious that the optimized structure shows a more instantaneous performance than the ordinary structure and it consumes a relatively lower pumping power.

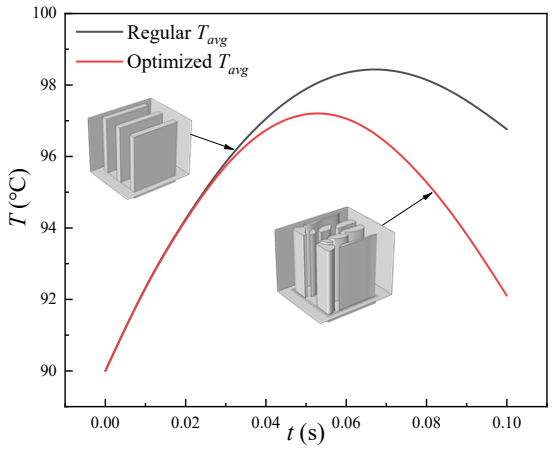

Fig. 33. Average base plate temperature of optimized and reference heat sink.

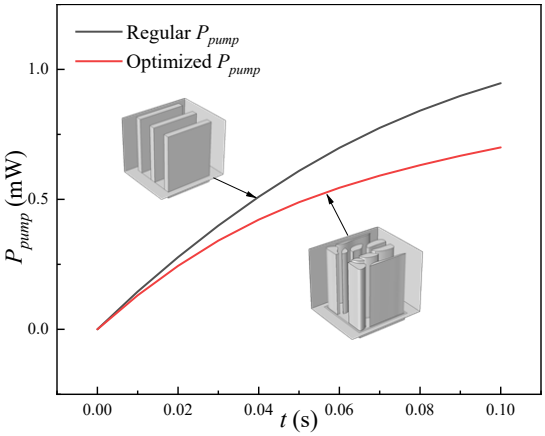

Fig. 34. Pumping power of optimized and reference heat sink.

Quasi-steady state comparison

Although the optimized structure performs better instantaneously, while being more energy-efficient, the quasi-steady performance must also be compared with the reference heat sink. The time interval is extended to 200s, which is used to ensure that models can reach quasi steady state. Thus, the average baseplate temperature of the two models are shown in Fig. 35, from which the steady-state temperature of the optimized design is around 5°C lower than the reference design. In comparison to the previous example using air, it is observed that the temperature will decrease below the turbo limit temperature of 90°C after approximately 0.11 seconds. In Fig. 35, when the average temperature reaches 55°C, which is an assumed lower limit temperature in this section to study their rising temperature procedure, the cooling time period t_c of each model are acquired: $t_{c,opt}$ and $t_{c,reg}$ respectively. In Fig. 36, pumping powers between 0 and 200s of optimized and reference heat sink are also compared, in which there are optimized and reference heat sink pumping power converging to 0.964mW and 1.47mW. Therefore, the optimized heat sink can achieve a lower quasi-state temperature with a relative lower pumping power.

Fig. 36 shows a small peak in pumping power curve at around 0.2s. This is because the inlet velocity increases to the peak and then decreases slightly to a steady state. This happens due to the instantaneous constant pressure inlet condition close to the design combined with the optimized design features[2].

[2] Mesh dependency can be excluded, because the peak still exist on subsequently finer meshes.

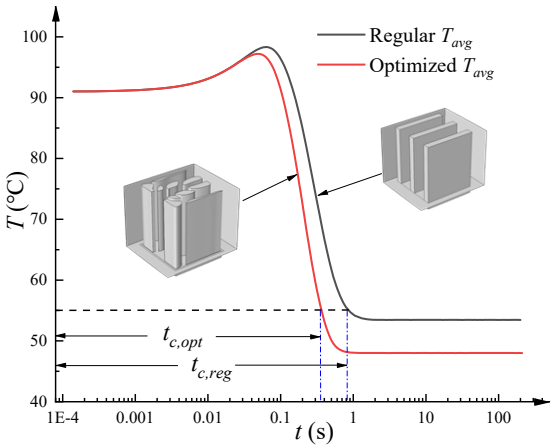

Fig. 35. Average base plate temperature of the optimized and reference heat sink.

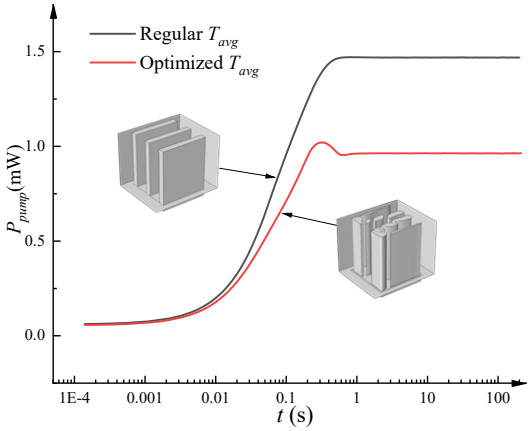

Fig. 36. Pumping power of the optimized and reference heat sink

Comparison on practical conditions

As the working conditions above are very ideal and have high energy consumption, a more practical setup is introduced. There are now two critical temperature limits: 90°C and 55°C. When the average temperature of the baseplate that is usually probed by sensors in the CPU chips, reaches 90°C, the cooling system will activate. During operation, a pressure of 50Pa is imposed on the inlet. With the increasing pumping power, the flow in the channel is accelerated, which leads to a constant decrease in the baseplate temperature. When the temperature then decrease to 55°C, the cooling system stops. Obviously, the temperature will rise back to 90°C again, and the cooling system will be activated with the whole procedure repeated.

The simulation results for the optimized and reference designs under such working conditions are shown in Fig. 37. It can be seen that the cooling time of the optimized model, $t_{c,opt}$ = 0.36s, is faster than the cooling time of the reference design, $t_{c,reg}$ = 0.82s. In terms of heating time, the optimized design has a very close result to the reference

design: $t_{ht,opt}$ = 1.55s versus $t_{ht,reg}$ = 1.54s. This is likely because the two designs have similar mass and thus a similar thermal mass.

In terms of pumping power, the total energy that two designs require is calculated with the formulation as follows:

$$E = \int_{t_c} P_{pump} dt \tag{44}$$

where t_c represents the cooling time period. Thus, the pumping energy that the designs consume shown in Fig. 37 can be obtained as: $E_{opt} = 0.28\times10^{-3}$ J versus $E_{reg} = 1.04\times10^{-3}$ J. The working period of the optimized design lasts 1.913s and the reference design lasts 2.367s. Therefore, the equivalent average energy consumption rate of the two designs are $ES_{opt} = 0.146\times10^{-3}$ J/s and $ES_{reg} = 0.439\times10^{-3}$ J/s. From this, it can be concluded that the optimized design can save 66.7% of the pumping energy of the reference design over the same time period.

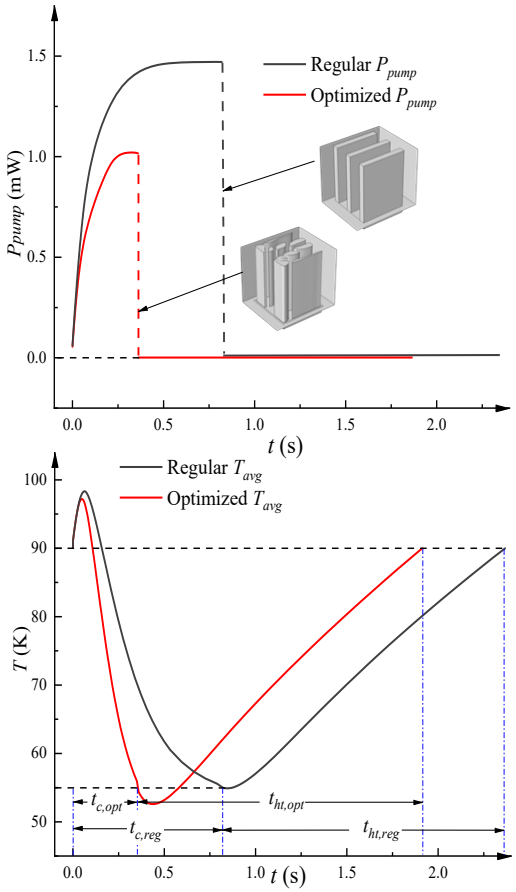

Fig. 37. Performances of two models in a period

5.4. Reynolds number of the air and water coolant model

The Reynolds number of the two different coolant models are shown in Fig. 38 with

respect to the time. The 4 models refer to the air coolant reference model in Fig. 1, air coolant optimized 4th model in Fig. 20, water coolant reference and optimized model in Fig. 33, respectively. Reynolds number of the air coolant model ranges from 140 to 210. However, as to the water coolant models, the number ranges from 2000 to 3400. Besides, the optimized model shows a better thermal performance with a lower flow velocity according to Fig. 20, Fig. 35 and Fig. 38.

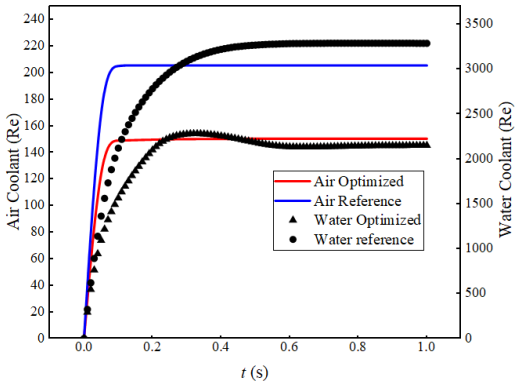

Fig. 38. Reynolds number of air and water coolant models

6. Conclusions

In this work, a transient pseudo-3D simulation and optimization model is introduced to provide a low computational cost method to fulfill the transient heat flow topology optimization process of 3D models. The optimization of pseudo-3D heat sinks has much lower manufacturing and processing requirements due to their extruded shape.

Although the transient pseudo-3D model is an approximate model of full 3D one, the proposed method provides a no more than 1% error of base plate temperature profile according to the introduced criterion. The proposed method mainly relies on the introduction of an artificial heat convection coefficient to establish the approximate relationship between pseudo 3D and full 3D. Thus the value of the heat convection coefficient decides the accuracy of pseudo-3D model. The value of the heat convection coefficient can be obtained by Eq. (15)-(19) in the full 3D simulation.

Besides, the detailed investigation of interpolation parameters and the choice of monotonously increasing interpolation curves assure a result with less intermediate density.

With the choice of the proper initial design, the optimization algorithm (GCMMA) can locate a better local optimum and achieve better instantaneous thermal performance.

Not only can the transient pseudo-3D model help to improve instantaneous performance

but also reduce the pumping power consumption to some extent (66.7% of the reduction rate of pumping power in Section 5.3).

Steady-state optimization has been shown to be incapable of replacing the transient analysis if a better instantaneous thermal performance is desired.

The inlet conditions set in this study are constant with respect to time, which means that the model may not be well adapted to real transient conditions, such as oscillating inlet pressure and time-dependent thermal generation. Treating these conditions is the subject of future work and should be treated in a similar framework as long as the penalty factors are investigated for the truly transient conditions.

Conflict of interest

The authors declare that there is no conflict of interest.

Acknowledgements

The first and second author have been supported by Project of the Key Program of National Natural Science Foundation of China under the Grant Numbers 11572120.

Appendix A. Mesh independency

A detailed mesh independency analysis of the transient pseudo 3D model and full 3D model is given in this appendix. The pseudo 3D model mesh independency strategy is implemented in the model shown in Fig. 14 and Fig. 30. The strategy is designed to compare the Degree Of Freedom (DOF) of a structured mesh with an unstructured mesh and further illustrate the reason why the mesh type has been changed in Fig. 29 of practical model. As for the 3D model mesh independency analysis, the heat convection coefficients h_f and h_s of the reference design shown in Fig. 1 is demonstrated with respect to the different DOFs. Furthermore, a mesh dependency analysis of the optimized 3D models is also made.

A.1. Reference 3D model mesh

The mesh dependency of the 3D reference model is investigated by calculating the heat convection coefficients h_s and h_f to illustrate whether it is accurate enough to be used for the optimization studies. It can be seen from Fig. 39 that the error between the previously used values and the converged values of the h_f and h_s of the original model are 1.35% and 0.091% respectively. The reason why we choose $h_s = 6.5\times10^4$ as the heat convection coefficient value is that the temperature difference between the base plate and the fins is quite small at the beginning of the transient. It might result in quite large value of h_s reaching up to 3.8×10^8, then plunge to less than 10^5 within just 0.2s and then gradually becomes stable at the level of 6.5×10^4. Since the heat convection coefficient in the solid material is considered to be a constant, the final value of the h_s adopted in topology optimization is the steady-state value 6.5×10^4 shown in Fig. 40.

A.2. Pseudo 3D model

The main reason for the change of the mesh type is to reduce the computational cost and maintain the accuracy. Two kinds of meshes are compared: structured and unstructured meshes in Fig. 41. In Fig. 42, it can be seen that the accuracy of the structured mesh is higher with the same DOFs and the base plate average temperature converges to 361.4K with the increase of DOF. Thus, the structured mesh was considered to have a higher accuracy with the same DOFs. Moreover, the original simulation FE model in Fig. 29 shows an error of 8.817×10^{-4}. Furthermore, the unstructured mesh model has slightly fluctuation even with a great number of DOFs. In summary, these are the reasons why the unstructured mesh is replaced with structured mesh.

A.3. Optimized design models

To validate the mesh independency of the optimized result, we compared different meshes for the optimized design using both the air and water as a coolant. As shown in Fig. 43, the air coolant “Optimized 4” design in Fig. 20 shows an error of 2.72×10^{-5}. The water coolant “Optimized” model in Fig. 33 shows an error of 5.86×10^{-3} in Fig. 44.

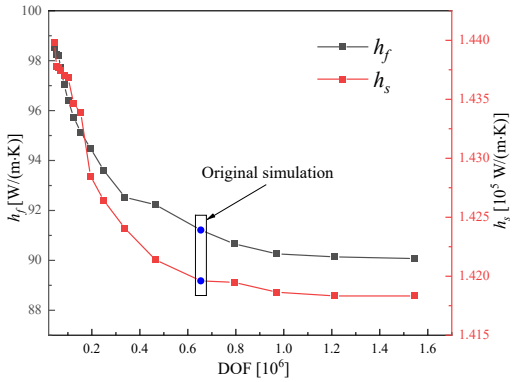

Fig. 39. Value of h_s and h_f in reference model

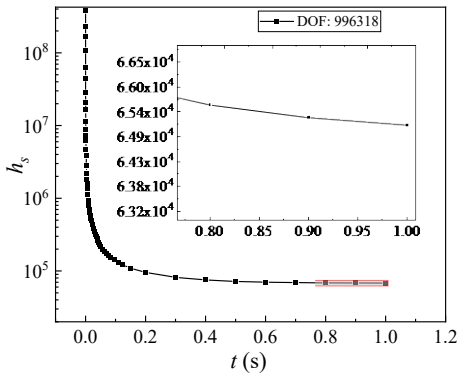

Fig. 40. h_s of reference model with respect to time with 996318 DOFs

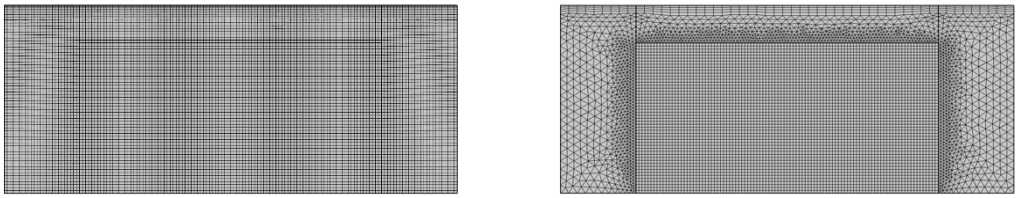

Fig. 41. Original structured mesh in manuscript (Left) and unstructured mesh.

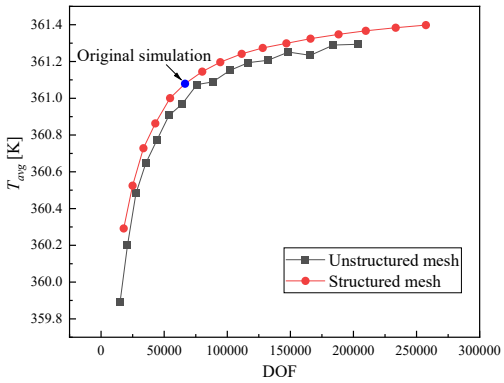

Fig. 42. Average temperature of base plate in unstructured and structured model

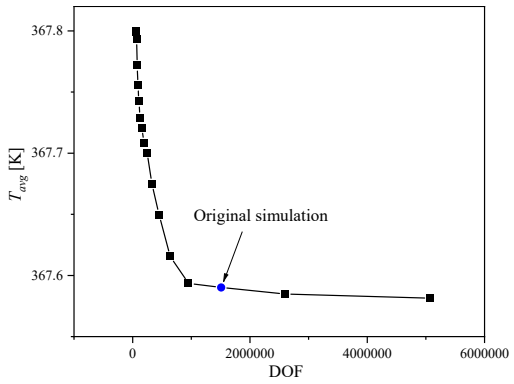

Fig. 43. T_{avg} of "Optimized 4th" in Fig. 20 3D model varies with respect to DOF

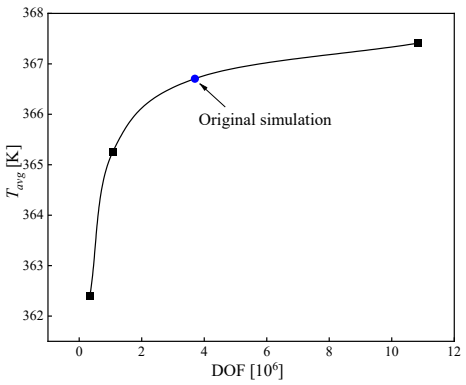

Fig. 44. T_{avg} of "Optimized" 3D model in Fig. 33 varies with respect to DOF

Appendix B. Implementation COMSOL Multiphysics

The whole topology optimization process is implemented in the commercial finite element software COMSOL Multiphysics. The general introduction of the software package can be found in Ref. [54]. The optimization model in COMSOL is composed of 5 modules:

a) PDE filter with boundary condition
b) Heat Transfer in Solids and Fluids
c) Laminar Flow
d) Heat Equation
e) Optimization

Each module has its own functions and meanings. For instance, the "*PDE filter with boundary conditions*" module is added manually using a reaction-diffusion equation to allow for fluid boundary conditions in the filter at the interface between design domain and fluid flow (density of nodes on the boundaries equal to 1). The second module contains all the thermal conducting, source and isolation boundaries. The conjugate heat transfer process is setup through this "*Heat Transfer in Solids and Fluids*" module. The 3rd module called "*Laminar Flow*" describes the laminar flow in the channel layer in Fig. 3. In this module, fluid flow boundaries such as no-slip boundaries, pressure inlet and outlets are prescribed. The 4th module used in this model is "Heat Equation", which is applied as the heat transfer calculation in base plate layer. This module mainly consists of description of "*Heat Equation*", "*Zero Flux*" and "Initial Values". The final

module "*Optimization*" is made up of terms named "*Integral Objective*" and "*Integral Inequality Constraint*". All of those modules are built-in physical field interfaces.

The special settings in the model that allows for the setup of the transient pseudo 3D model are the heat source terms. In the "*Heat Transfer in Solids and Fluids*" module, the volumetric thermal generation in "*Heat Source*" term is set to $h(\theta)(T_{bp}-T)/t_{ch}$ as formulated in Eq. (32), which means that the value of heat source is determined by the temperature difference between base plate temperature and temperature in channel layer as well as the heat artificial convection coefficient $h(\theta)$. Further, in the "*Heat Equation*" module the source term should subtract the heat that is transferred from the base plate to the heat sink fins on the basis of original chip power, which denotes as $Q/V_{bp}-h(\theta)(T_{bp}-T)/t_{bp}$ formulated in Eq. (34).

References

[1] S. Zeng, P.S. Lee, Topology optimization of liquid-cooled microchannel heat sinks: An experimental and numerical study, Int. J. Heat Mass Transf. 142 (2019) 118401. https://doi.org/https://doi.org/10.1016/j.ijheatmasstransfer.2019.07.051.

[2] Intel® Core™ i9-9900K Processor (16M Cache, up to 5_00 GHz) 186605, (n.d.). https://doi.org/https://www.intel.com/content/www/us/en/products/processors/core/i9-processors/i9-9900k.html.

[3] Y.J. Lee, P.S. Lee, S.K. Chou, Enhanced Thermal Transport in Microchannel Using Oblique Fins, J. Heat Transfer. 134 (2012) 101901. https://doi.org/10.1115/1.4006843.

[4] Y. Sui, C.J. Teo, P.S. Lee, Y.T. Chew, C. Shu, Fluid flow and heat transfer in wavy microchannels, Int. J. Heat Mass Transf. 53 (2010) 2760–2772. https://doi.org/10.1016/j.ijheatmasstransfer.2010.02.022.

[5] Z.L. Chiam, P.S. Lee, P.K. Singh, N. Mou, Investigation of fluid flow and heat transfer in wavy micro-channels with alternating secondary branches, Int. J. Heat Mass Transf. 101 (2016) 1316–1330. https://doi.org/10.1016/j.ijheatmasstransfer.2016.05.097.

[6] A. Bejan, M.R. Errera, Convective trees of fluid channels for volumetric cooling, Int. J. Heat Mass Transf. 43 (2000) 3105–3118. https://doi.org/10.1016/S0017-9310(99)00353-1.

[7] D. Pence, Reduced pumping power and wall temperature in microchannel heat sinks with fractal-like branching channel networks, Microscale Thermophys. Eng. 6 (2003) 319–330. https://doi.org/10.1080/10893950290098359.

[8] Y. Chen, P. Cheng, Heat_Transfer_and_Pressure_Drop_in_Fractal_Tree-Li.pdf, Int. J. Heat Mass Transf. 45 (2002) 2643–2648.

[9] C.S. Sharma, G. Schlottig, T. Brunschwiler, M.K. Tiwari, B. Michel, D. Poulikakos, A novel method of energy efficient hotspot-targeted embedded liquid cooling for electronics: An experimental study, Int. J. Heat Mass Transf. 88 (2015) 684–694. https://doi.org/10.1016/j.ijheatmasstransfer.2015.04.047.

[10] R. Hilbert, G. Janiga, R. Baron, D. Thévenin, Multi-objective shape optimization of a heat exchanger using parallel genetic algorithms, Int. J. Heat Mass Transf. 49 (2006) 2567–2577. https://doi.org/10.1016/j.ijheatmasstransfer.2005.12.015.

[11] M.P.B. E, Generating Optimal Topologies in Structural, Comput. Methods Appl. Mech. Eng. 71 (1988) 197–224.

[12] O. Sigmund, K. Maute, Topology optimization approaches: A comparative review, Struct. Multidiscip. Optim. (2013). https://doi.org/10.1007/s00158-013-0978-6.

[13] M.P. Bendsøe, Optimal shape design as a material distribution problem, Struct. Optim. 1 (1989) 193–202. https://doi.org/10.1007/BF01650949.

[14] M. Zhou, G.I.N. Rozvany, The COC algorithm, Part II: Topological, geometrical and generalized shape optimization, Comput. Methods Appl. Mech. Eng. 89 (1991) 309–336. https://doi.org/10.1016/0045-7825(91)90046-9.

[15] M.Y. Wang, X. Wang, D. Guo, A level set method for structural topology optimization, Comput. Methods Appl. Mech. Eng. 192 (2003) 227–246. https://doi.org/10.1016/S0045-7825(02)00559-5.

[16] G. Allaire, F. Jouve, A.-M. Toader, Structural optimization using sensitivity analysis and a level-set method, J. Comput. Phys. 194 (2004) 363–393. https://doi.org/10.1016/j.jcp.2003.09.032.

[17] Q. Xia, M.Y. Wang, T. Shi, A level set method for shape and topology optimization of both structure and support of continuum structures, Comput. Methods Appl. Mech. Eng. (2014). https://doi.org/10.1016/j.cma.2014.01.014.

[18] Q. Xia, M.Y. Wang, T. Shi, Topology optimization with pressure load through a level set method, Comput. Methods Appl. Mech. Eng. (2015). https://doi.org/10.1016/j.cma.2014.09.022.

[19] S. Kreissl, K. Maute, Levelset based fluid topology optimization using the extended finite element method, Struct. Multidiscip. Optim. 46 (2012) 311–326. https://doi.org/10.1007/s00158-012-0782-8.

[20] Y.M. Xie, G.P. Steven, A simple evolutionary procedure for structural optimization, Comput. Struct. (1993). https://doi.org/10.1016/0045-7949(93)90035-C.

[21] Q. O.M., Evolutionary structural optimisation (ESO) using a bidirectional algorithm, Eng. Comput. 15 (1998) 1031–1048. https://doi.org/10.1108/02644409810244129.

[22] J.D. Deaton, R. V. Grandhi, A survey of structural and multidisciplinary continuum topology optimization: Post 2000, Struct. Multidiscip. Optim. 49 (2014) 1–38. https://doi.org/10.1007/s00158-013-0956-z.
[23] L. Yin, G.K. Ananthasuresh, A novel topology design scheme for the multi-physics problems of electro-thermally actuated compliant micromechanisms, Sensors Actuators A Phys. 97–98 (2002) 599–609. https://doi.org/https://doi.org/10.1016/S0924-4247(01)00853-6.
[24] A. Iga, S. Nishiwaki, K. Izui, M. Yoshimura, Topology optimization for thermal conductors considering design-dependent effects, including heat conduction and convection, Int. J. Heat Mass Transf. 52 (2009) 2721–2732. https://doi.org/https://doi.org/10.1016/j.ijheatmasstransfer.2008.12.013.
[25] Y. Joo, I. Lee, S.J. Kim, Topology optimization of heat sinks in natural convection considering the effect of shape-dependent heat transfer coefficient, Int. J. Heat Mass Transf. 109 (2017) 123–133. https://doi.org/10.1016/j.ijheatmasstransfer.2017.01.099.
[26] T.E. Bruns, Topology optimization of convection-dominated, steady-state heat transfer problems, Int. J. Heat Mass Transf. 50 (2007) 2859–2873. https://doi.org/10.1016/j.ijheatmasstransfer.2007.01.039.
[27] J. Alexandersen, Topology Optimization for Convection Problems, 2011. https://doi.org/10.13140/RG.2.2.24635.72485.
[28] M. Zhou, J. Alexandersen, O. Sigmund, C.B. W. Pedersen, C.B. Claus, Industrial application of topology optimization for combined conductive and convective heat transfer problems, Struct. Multidiscip. Optim. 54 (2016) 1045–1060. https://doi.org/10.1007/s00158-016-1433-2.
[29] B. Lazarov, J. Alexandersen, O. Sigmund, Topology Optimized Designs of Steady State Conduction Heat Transfer Problems with Convection Boundary Conditions, 2014. https://doi.org/10.13140/RG.2.2.29361.68966.
[30] C. Wang, X. Qian, A Density Gradient Approach to Topology Optimization Under Design-Dependent Boundary Loading, (2018). https://doi.org/10.1115/DETC2018-85960.
[31] E. Dede, Multiphysics Topology Optimization of Heat Transfer and Fluid Flow Systems, 2009.
[32] G. Yoon, Topological design of heat dissipating structure with forced convective heat transfer, J. Mech. Sci. Technol. 24 (2010) 1225–1233. https://doi.org/10.1007/s12206-010-0328-1.
[33] T. Dbouk, A review about the engineering design of optimal heat transfer systems using topology optimization, Appl. Therm. Eng. 112 (2016) 841–854. https://doi.org/10.1016/j.applthermaleng.2016.10.134.
[34] C. Dilgen, S. Dilgen, D. Fuhrman, O. Sigmund, B. Lazarov, Topology optimization of turbulent flows, Comput. Methods Appl. Mech. Eng. 331 (2017). https://doi.org/10.1016/j.cma.2017.11.029.
[35] J. Alexandersen, N. Aage, C.S. Andreasen, O. Sigmund, Topology optimisation for natural convection problems, Int. J. Numer. Methods Fluids. 76 (2014) 699–721. https://doi.org/10.1002/fld.3954.
[36] J. Alexandersen, O. Sigmund, N. Aage, Large scale three-dimensional topology optimisation of heat sinks cooled by natural convection, Int. J. Heat Mass Transf. 100 (2016) 876–891. https://doi.org/10.1016/j.ijheatmasstransfer.2016.05.013.
[37] J. Alexandersen, O. Sigmund, K. Erik, B. Stefanov, International Journal of Heat and Mass Transfer Design of passive coolers for light-emitting diode lamps using topology optimisation, Int. J. Heat Mass Transf. 122 (2018) 138–149. https://doi.org/10.1016/j.ijheatmasstransfer.2018.01.103.
[38] Y. Joo, I. Lee, S.J. Kim, Efficient three-dimensional topology optimization of heat sinks in natural convection using the shape-dependent convection model, Int. J. Heat Mass Transf. (2018). https://doi.org/10.1016/j.ijheatmasstransfer.2018.08.009.
[39] J. Asmussen, J. Alexandersen, O. Sigmund, C. Andreasen, A “poor man’s” approach to topology optimization of natural convection problems, Struct. Multidiscip. Optim. (2019). https://doi.org/10.1007/s00158-019-02215-9.
[40] N. Pollini, O. Sigmund, C.S. Andreasen, J. Alexandersen, A “poor man’s” approach for high-resolution three-dimensional topology optimization of natural convection problems, (n.d.).
[41] J.H.K. Haertel, K. Engelbrecht, B.S. Lazarov, O. Sigmund, Topology optimization of a pseudo 3D thermofluid heat sink model, Int. J. Heat Mass Transf. 121 (2018) 1073–1088. https://doi.org/10.1016/j.ijheatmasstransfer.2018.01.078.
[42] S. Zeng, B. Kanargi, P.S. Lee, Experimental and numerical investigation of a mini channel forced air heat sink designed by topology optimization, Int. J. Heat Mass Transf. 121 (2018) 663–679. https://doi.org/10.1016/j.ijheatmasstransfer.2018.01.039.
[43] S. Yan, F. Wang, J. Hong, O. Sigmund, Topology optimization of microchannel heat sinks

using a two-layer model, Int. J. Heat Mass Transf. 143 (2019) 118462. https://doi.org/10.1016/j.ijheatmasstransfer.2019.118462.
[44] T. Indinger, I. V Shevchuk, Transient laminar conjugate heat transfer of a rotating disk: theory and numerical simulations, Int. J. Heat Mass Transf. 47 (2004) 3577–3581. https://doi.org/https://doi.org/10.1016/j.ijheatmasstransfer.2004.01.023.
[45] I. V Shevchuk, Unsteady conjugate laminar heat transfer of a rotating non-uniformly heated disk: Application to the transient experimental technique, Int. J. Heat Mass Transf. 49 (2006) 3530–3537. https://doi.org/https://doi.org/10.1016/j.ijheatmasstransfer.2006.03.001.
[46] Z. Zhou, X. Xu, X. Liang, Experiments on the transient heat transfer of minichannel heat sink under high heat flux density in an enclosed loop, Exp. Therm. Fluid Sci. 34 (2010) 1409–1414. https://doi.org/https://doi.org/10.1016/j.expthermflusci.2010.07.001.
[47] T. Borrvall, J. Petersson, Topology optimization of fluids in Stokes flow, Int. J. Numer. Methods Fluids. 41 (2003) 77–107. https://doi.org/10.1002/fld.426.
[48] J. Alexandersen, Topology Optimisation for Coupled Convection Problems, 2013. https://doi.org/10.13140/RG.2.2.31346.61129.
[49] C. Lundgaard, J. Alexandersen, M. Zhou, C.S. Andreasen, O. Sigmund, Revisiting density-based topology optimization for fluid-structure-interaction problems, Struct. Multidiscip. Optim. 58 (2018) 969–995. https://doi.org/10.1007/s00158-018-1940-4.
[50] O. Sigmund, J. Petersson, Numerical instabilities in topology optimization: A survey on procedures dealing with checkerboards, mesh-dependencies and local minima, Struct. Optim. 16 (1998) 68–75. https://doi.org/10.1007/BF01214002.
[51] COMSOL, COMSOL Multiphysics 5.4, 2018.
[52] J.H.K. Haertel, K. Engelbrecht, B.S. Lazarov, O. Sigmund, Topology optimization of a pseudo 3D thermofluid heat sink model, Int. J. Heat Mass Transf. 121 (2018) 1073–1088. https://doi.org/10.1016/j.ijheatmasstransfer.2018.01.078.
[53] B.S. Lazarov, O. Sigmund, K.E. Meyer, J. Alexandersen, Experimental validation of additively manufactured optimized shapes for passive cooling, Appl. Energy. 226 (2018) 330–339. https://doi.org/https://doi.org/10.1016/j.apenergy.2018.05.106.
[54] COMSOL, Introduction to COMSOL Multiphysics, 2019. https://www.comsol.com/offers/intro-to-multiphysics.